Accurate Impedance Modeling and Control Strategy for Improving the Stability of DC System in Multiterminal MMC-Based DC Grid

Zhenyu Li, Zhang Wang, Yue Wang, *Member, IEEE*, Taiyuan Yin, Nian Mei, Bo Yue, and Wanjun Lei, *Member, IEEE*

***Abstract*—This article proposes an accurate dc-side impedance modeling method of modular multilevel converter (MMC) and a control strategy for improving the stability of the dc system in MMC-based dc grid. First, the impedance modeling method based on harmonic linearization is adopted to establish the dc-side small-signal impedance model of MMC, which considers the internal multiharmonic coupling characteristics and the complete control system. Second, an equivalent model is established to analyze the frequency impedance characteristics of the dc ports in MMC-based dc grid, and the stability of dc ports is further analyzed based on the impedance-based stability criterion. Then, considering both the dynamic characteristics and stability of the dc system, a specific design method of controller parameter optimization and additional virtual damping controller is proposed. Based on MATLAB/Simulink, a detailed time-domain simulation model of MMC-based dc grid is established. The simulation results prove the accuracy of the proposed impedance modeling method and the validity of the proposed control strategy.**

***Index Terms*—Frequency impedance characteristic, harmonic linearization, impedance model, modular multilevel converter (MMC)-based dc grid, virtual damping.**

I. Introduction

In RECENT years, modular-multilevel-converter-based high-voltage direct current transmission technology (MMC-HVdc) has become an ideal solution for the power transmission of island new energy electric field due to its advantages, such as high modularity, low switching loss, small output voltage distortion, and active and reactive power decoupling control [1], [2]. However, with the establishment of more and more MMC-HVdc projects, its potential stability problem becomes more and more prominent. For MMC-based dc grid with large capacity, its stability problem is more prominent. MMC-based dc grid is a complex system due to its multiple ports. Harmonic of any ac port may flow into the MMC-based dc grid through MMC, causing resonance of the whole dc grid.

Past research on the voltage source converter (VSC) shows that both impedance-based and eigenvalue-based stability analysis methods can be used to analysis the stability of the system for a VSC-based HVdc system [3], [4], and the ac-side and dc-side impedance coupling relationship is analyzed in detail in [5]. From previous research works, the dc-side impedance model of VSC, including control loops, is derived, and the stability of VSC-HVdc is studied based on the impedance model [6]–[9].

At present, there have been some research works on the stability of VSC-based HVdc system and ac system in MMC-based dc grid in the engineering, whereas rare research works on the stability of dc system are done. In this article, the way to study the stability of the dc system is to analyze stability of dc ports based the impedance-based stability criterion [10]–[12], which first requires obtaining the frequency impedance characteristics of each dc port. However, because of its complex internal structure and special circulation controller, dc-side impedance modeling of MMC is much more complicated than the two-level VSC [13]–[16]. The topology of the MMC-based dc grid is diverse, and the connection mode of the dc system is complex, so the transformation of operating mode will change the frequency impedance characteristics of the dc ports. In addition, the frequency impedance characteristics of dc ports are much more complicated due to the use of overhead lines. So, it is very difficult to study the stability of the dc system in MMC-based dc grid.

From previous research work, it is universally acknowledged that mastering the dc-side frequency impedance characteristics of MMC is the key to study the stability of the dc system in MMC-based dc grid. Generally, the frequency impedance characteristics can be obtained by the simulation measurement and the impedance modeling. The simulation measurement needs to build a detailed simulation model and test the impedance of multiple frequencies, which is time-consuming and needs to be retested when the system parameters change, whereas the

Manuscript received June 19, 2019; revised September 8, 2019, November 18, 2019, and January 7, 2020; accepted February 12, 2020. Date of publication February 24, 2020; date of current version June 23, 2020. This work was supported by Science and Technology Projects of State Grid Corporation of China under Grant 52010118000B. Recommended for publication by Associate Editor X. Wang. *(Corresponding author: Yue Wang.)*

Zhenyu Li is with State Grid Corporation of China, Beijing 100031, China (e-mail: zhenyu-li@sgcc.com.cn).

Zhang Wang, Yue Wang, Taiyuan Yin, and Wanjun Lei are with the School of Electrical Engineering, Xi'an Jiao tong University, Xi'an 710049, China (e-mail: wangzhang@stu.xjtu.edu.cn; davidewangyue@mail.xjtu.edu.cn; yintaiyuan945@126.com; leiwanjun@xjtu.edu.cn).

Nian Mei and Bo Yue are with State Grid Economic and Technological Research Institute Co., Ltd., Beijing 102209, China (e-mail: meinn@126.com; yuebo2000@163.com).

Color versions of one or more of the figures in this article are available online at http://ieeexplore.ieee.org.

Digital Object Identifier 10.1109/TPEL.2020.2975619

principle of impedance modeling is to establish the impedance model of the MMC through analytical calculation, which is convenient and fast, and can study the influence of various system parameters on the frequency impedance characteristics. Therefore, it is more suitable to obtain the frequency impedance characteristics of the MMC on dc side. In [17]–[19], the average model of MMC is deduced for analyzing terminal behaviors. However, its derivation directly ignores the coupling of multiple harmonics within arms and the dynamic process of the submodule capacitor, so it cannot accurately reflect the actual characteristics of the MMC. In [20] and [21], the dc-side small-signal impedance model of MMC is proposed, in which the influence of circulating current control is considered. However, the influence of inner and outer loop controllers on dc-side impedance has not been analyzed, so the obtained model is not general. In [22], the dc-side impedance model of MMC is established and the resonance mechanism of the dc ports in MMC-based dc grid is analyzed. In addition, the stabilization strategy was proposed by using capacitor energy storage effect to suppress the harmonics on the dc side and to avoid the resonance of the dc system. However, the established MMC dc-side impedance model is an inductor, which directly ignores the characteristics of the submodule capacitor and the influence of control system, resulting in a low accuracy of the model. The sequence impedance model on the ac side of MMC based on the harmonic linearization is established in [23]. In the model, the coupling among multiple harmonics within MMC and the dynamic process of submodule capacitor were considered. With high accuracy, it can be directly extended to the impedance modeling on the dc side of MMC. However, the small-signal model of the outer-loop controller is not considered in the modeling. The impedance model on the ac side of MMC based on the harmonic state space (HSS) modeled with voltage control loop is established in [25] and [26]. And the zero-sequence voltage in ac side caused by the inner coupling of MMC is further considered in the single-phase model of MMC with current control in [27]. But they all only consider single closed-loop control in the model, whereas the double closed-loop control strategy and different control modes commonly used in engineering are not covered [25]–[27]. In [28], the dc-side impedance model of MMC based on the HSS modeling is established without considering the influence of the control system. In fact, the actual MMC is a closed-loop controlled system, and thus the established model is incomplete.

In addition, additional virtual damping controller is often used to improve the stability of the dc system in the MMC-HVdc project. However, due to the low accuracy of the established impedance model, it has certain limitations in the design process of the parameters of the virtual damping controller. For Maritime VSC-HVdc system, the method of additional virtual series damping on the dc side of converter station under dc voltage control mode is proposed to suppress the resonance of dc system in [29], and the influence of different virtual damping controller parameters on the stability of the system by the Nyquist criterion is analyzed. In [30], additional virtual damping controller on the dc side of converter station under power control mode is proposed to improve the stability of the dc ports in the MMC-HVdc system, and it gives the detailed parameter design process of the virtual damping controller. However, the average model for the MMC is adopted in the analysis of frequency impedance characteristics, with low accuracy. In addition, the filters in the virtual damping controller are band filter, which will make the dynamic performance of the system worse. An ac impedance model for grid-connected MMCs by means of complex vectors and harmonic transfer function matrices is developed, and the impacts of the zero-sequence circulating current (ZSCC) control on the ac-side dynamics of the MMC are revealed in [31]. A systematic parameter-tuning guideline for the ZSCC control loop is also developed. Based on the abovementioned analysis, it is necessary to establish a more accurate MMC dc-side small-signal impedance model to analyze the stability of the dc port in MMC-based dc grid and propose the corresponding stabilization method.

In this article, the control strategy to improve the stability of the dc system in multiterminal MMC-based dc grid is studied. First, based on harmonic linearization, a small-signal impedance model of MMC on dc side is established, which considers the coupling of internal multiple harmonics and the complete control system. As a result, the established impedance model is highly accurate. Second, taking a typical four-terminal MMC-based dc grid as an example, the stability of each dc port is studied based on the impedance stability criterion. Then, aiming at the problem of insufficient stability margin in the abovementioned analysis results, the stabilization strategy of optimizing controller parameters and adding virtual damping controller is adopted. Considering both the dynamic characteristics and stability of the system, the precise design method of optimizing controller parameters and adding virtual damping controller is proposed. Finally, the simulation results verify the effectiveness of the proposed control strategy and provide a reference for improving the stability of the dc system in MMC-based dc grid.

II. Small-Signal Model of MMC Power Stage

A. Averaged Model

Fig. 1 shows the circuit diagram of an MMC. Each arm consists of *N* submodules, and each electrical variable uses two subscripts, which designate the phase (a, b, and c) and the arm (*u* for the upper arm, and *l* for the lower arm), respectively. In addition, L is the inductance of the arm inductor, and its equivalent parasitic resistance is r_L. C_m is the capacitance of the submodule capacitor. Assuming that the insertion index of upper arm of phase a is m_{au}, and all submodule voltages are balanced, time-domain averaged model of upper arm of phase a can be expressed as (1) and (2) [32], [33]

$$L\frac{di_{au}}{dt} + r_L i_{au} = v_p - v_a - m_{au}v_{au} \tag{1}$$

$$C\frac{dv_{au}}{dt} = m_{au}i_{au} \tag{2}$$

where v_a is voltage of phase a, i_{au} is the current of phase a upper arm, v_{au} is the sum of the capacitor voltages of all submodules in the phase a upper arm, and $C = C_m/N$ is the equivalent capacitance of all submodule capacitors. In addition, each electrical variable in the MMC contains multiple frequency

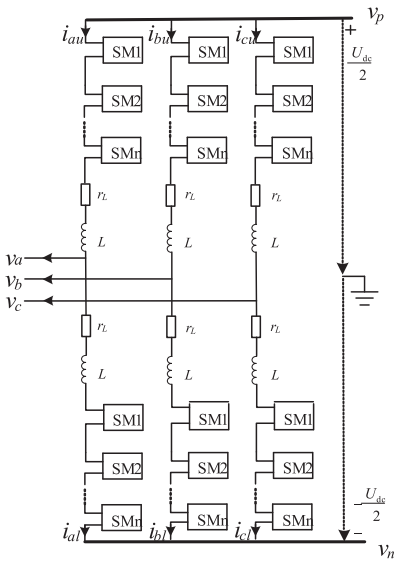

Fig. 1. Basic structure of MMC.

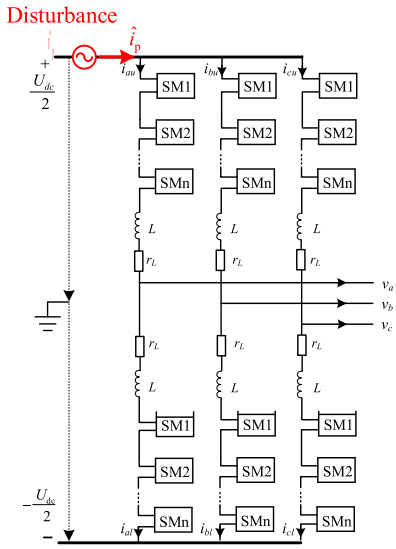

Fig. 2. Diagram of MMC with dc-side disturbance voltage.

components, and coupling relationship exists among electrical variables of different frequencies.

B. Linearization of Power Stage Model

Referring to [23], the way to model MMC dc-side impedance by harmonic linearization is to add a sinusoidal voltage perturbation on the dc side of the MMC first, which is shown in Fig. 2. And then, the dc-side impedance can be determined by calculating the corresponding dc-side current response at the perturbation frequency. Obviously, the dc bus voltage is

$$v_{pn} = V_{\rm dc} + \hat{v}_p = V_{\rm dc} + V_p \cos(2\pi f_p t + \varphi_p) \tag{3}$$

where v_{pn} is dc bus voltage when perturbation voltage is added, $\hat{v}_p$ is perturbation voltage, V_p is magnitude of perturbation voltage, and φ_p is phase angle of perturbation voltage.

Because the measurement of dc-side impedance is based on the linear and time-invariant circuits obtained after the linearization, it is independent from the initial phase angle of the voltage perturbation [33]. In order to facilitate the calculation, the initial phase angle can be set to zero.

Since there is a symmetrically similar relationship among three phases, the subscripts a, b, and c of variables which designate the phase are dropped to simplify the notation. The voltage perturbation $\hat{v}_p$ added to the dc side will lead to a small-signal harmonic response at the perturbation frequency in the arm current i_u, the sum of submodule capacitor voltages v_u, and the insertion index m_u, respectively. These small-signal harmonics are coupled with steady-state harmonics, which lead to a pair of new small-signal harmonics with frequency of $f_p \pm kf_1$, $k = 1, 2, \ldots, n$. At the same time, small-signal harmonics will also be coupled with each other to produce high-order small-signal harmonics with frequency of $mf \pm kf_1$, $k = 1, 2, \ldots, n$, $m = 1, 2, \ldots, n$. But their amplitudes are too small and can be ignored in the linearization [23]. Therefore, these small-signal harmonics generated by the voltage perturbation added to the MMC dc side can be represented as vectors.

In addition, since the voltage perturbation added on the dc side has the same effect on the six arms, the phase and sequence relationships among the harmonics of six arms can be expressed as follows [34]–[37].

Notably, the differential-mode components will flow to the ac side, the positive and negative common-mode components will flow among the three phase arms, and the zero common-mode components will flow to the dc side

$$\hat{v}_u = \begin{bmatrix} \hat{V}_{p-n}e^{j\hat{\alpha}_{p-n}} \\ \vdots \\ \hat{V}_{p-1}e^{j\hat{\alpha}_{p-1}} \\ \hat{V}_p e^{j\hat{\alpha}_p} \\ \hat{V}_{p+1}e^{j\hat{\alpha}_{p+1}} \\ \vdots \\ \hat{V}_{p+n}e^{j\hat{\alpha}_{p+n}} \end{bmatrix}, \quad \hat{i}_u = \begin{bmatrix} \hat{I}_{p-n}e^{j\hat{\beta}_{p-n}} \\ \vdots \\ \hat{I}_{p-1}e^{j\hat{\beta}_{p-1}} \\ \hat{I}_p e^{j\hat{\beta}_p} \\ \hat{I}_{p+1}e^{j\hat{\beta}_{p+1}} \\ \vdots \\ \hat{I}_{p+n}e^{j\hat{\beta}_{p+n}} \end{bmatrix},$$

$$\hat{m}_u = \begin{bmatrix} \hat{M}_{p-n}e^{j\hat{\gamma}_{p-n}} \\ \vdots \\ \hat{M}_{p-1}e^{j\hat{\gamma}_{p-1}} \\ \hat{M}_p e^{j\hat{\gamma}_p} \\ \hat{M}_{p+1}e^{j\hat{\gamma}_{p+1}} \\ \vdots \\ \hat{M}_{p+n}e^{j\hat{\gamma}_{p+n}} \end{bmatrix} \tag{4}$$

$$f = \begin{cases} f_p + 3kf_1 & \text{zero sequence} \\ f_p + (3k+1)f_1 & \text{positive sequence} \\ f_p + (3k-1)f_1 & \text{negative sequence} \end{cases}$$

$$f = \begin{cases} f_p + (2k+1)f_1 & \text{differential mode} \\ f_p + 2kf_1 & \text{common mode} \end{cases}. \tag{5}$$

Based on the abovementioned analysis, the power stage small-signal model of the MMC can be obtained after the linearization

of average model [38]–[41]

$$\boldsymbol{Z}_l\hat{i}_u = \hat{v}_p/2 - \hat{v}_a - \boldsymbol{m}_u \otimes \hat{v}_u - \boldsymbol{v}_u \otimes \hat{m}_u \tag{6}$$

$$\boldsymbol{Y}_c\hat{v}_u = \boldsymbol{M}_u\hat{i}_u + \boldsymbol{I}_u\hat{m}_u \tag{7}$$

where $\hat{i}_u$, $\hat{v}_u$,$\hat{m}_u$, and $\hat{v}_a$ are vectors of the small-signal harmonics, and $\boldsymbol{I}_u$, $\boldsymbol{V}_u$, and $\boldsymbol{M}_u$ are matrixes of steady-state variables. $\boldsymbol{I}_u$, $\boldsymbol{V}_u$, and $\boldsymbol{M}_u$ have similar matrix forms, and using the $\boldsymbol{V}_u$ as example, the corresponding steady-state matrix is

$$V_u = \begin{bmatrix} \ddots & \vdots & \vdots & \vdots & \vdots & \vdots & \iddots \\ \cdots & V_1e^{j\alpha_1} & V_0 & V_1e^{-j\alpha_1} & V_2e^{-j\alpha_2} & V_3e^{-j\alpha_3} & \cdots \\ \cdots & V_2e^{j\alpha_2} & V_1e^{j\alpha_1} & V_0 & V_1e^{-j\alpha_1} & V_2e^{-j\alpha_2} & \cdots \\ \cdots & V_3e^{j\alpha_3} & V_2e^{j\alpha_2} & V_1e^{j\alpha_1} & V_0 & V_1e^{-j\alpha_1} & \cdots \\ \iddots & \vdots & \vdots & \vdots & \vdots & \vdots & \ddots \end{bmatrix}. \tag{8}$$

In addition, the impedance of the arm inductor and the equivalent module capacitor are as follows:

$$\begin{aligned} Z_l = {} & j2\pi L \cdot \mathrm{diag}[f_p - nf_1, \cdots, f_p - f_1, f_p, \\ & f_p + f_1, \cdots, f_p + nf_1] \\ & + \mathrm{diag}\Big[r_L, \cdots, r_L, r_L, r_L, \cdots, r_L\Big] \\ Y_c = {} & j2\pi C \cdot \mathrm{diag}\,[f_p - nf_1, \cdots, f_p - f_1, f_p, \\ & f_p + f_1, \cdots, f_p + nf_1]. \end{aligned} \tag{9}$$

It is pointed out that the small-signal model considering three or more times of small-signal harmonics is accurate enough, so the modeling of small-signal impedance in this article only considers the harmonics within three times [23]. In addition, the small-signal harmonic vector of upper arm insertion index $\hat{m}_u$ is related to the control system mode and parameters. In order to get the small-signal impedance model, it is necessary to set up the small-signal model of the control system.

III. Control Modeling and DC-Side Impedance of MMC

The control modes of MMC mainly include dc voltage control, ac voltage control, and power control. In this section, the small-signal models of these three typical control modes will be established, respectively. In addition, the modeling process is similar to other control modes.

A. DC Voltage Control Mode

A typical MMC double-loop control block diagram of the dc voltage control mode is shown in Fig. 3. In general, it is equal to the superposition of four control loops [33], so the small-signal model of dc voltage control mode can be modeled by

$$\hat{m}_u = \boldsymbol{Q}_i\hat{i}_u + \boldsymbol{Q}_c\hat{i}_u + \boldsymbol{P}_v\hat{v}_p/2 + \boldsymbol{P}_{\mathrm{pll}}\hat{v}_a \tag{10}$$

where $\boldsymbol{Q}_i$, $\boldsymbol{Q}_c$, $\boldsymbol{P}_v$, and $\boldsymbol{P}_{\mathrm{pll}}$ are the coefficient matrixes of the phase current control loop, the circulating current control loop, the dc voltage control loop, and the phase lock loop,

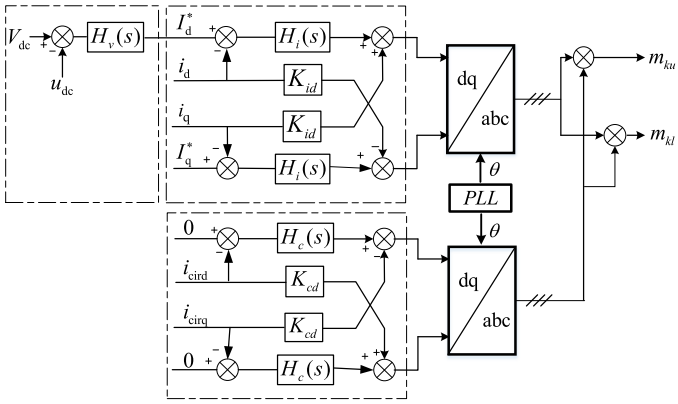

Fig. 3. Block diagram of dc voltage control mode.

respectively. In this article, only the harmonics within three times are considered, so $\boldsymbol{Q}_i$, $\boldsymbol{Q}_c$, $\boldsymbol{P}_v$, and $\boldsymbol{P}_{\mathrm{pll}}$ are all square matrices of seven order, and the matrix coefficients are related to their control loop and control parameters.

1) Phase Current Control: The phase current loop controls the three-phase ac terminal current, and only the positive- or negative-sequence components in the arm current of the differential mode can be output to the ac terminals. In other words, the phase current controller only works on current harmonics whose frequencies are $f = f_p + (6k \pm 1)f_1$, $k \in \mathrm{Z}$. Based on the abovementioned analysis, the coefficient matrix of the phase current control loop can be expressed as

$$\boldsymbol{Q}_i = \mathrm{diag}\,[0 \quad 0 \quad a \quad 0 \quad b \quad 0 \quad 0] \tag{11}$$

where the frequency corresponding to coefficient a is $f_p - f_1$, which is the gain coefficient of the negative-sequence component of the differential mode, whereas the frequency corresponding to coefficient b is $f_p + f_1$, which is the gain coefficient of the positive-sequence component of the differential mode.

Since the phase current loop adopts a proportional integral (PI) controller based on *dq* decoupling control, it is pointed out in [23] that *dq* transformation will shift the frequency downward by f_1 of positive-sequence harmonics and upward by f_1 for negative-sequence harmonics, where f_1 is the fundamental frequency. Thus, the parameters in the coefficient matrix $\boldsymbol{Q}_i$ can be obtained by

$$\begin{aligned} a &= H_i(j2\pi(f_p - f_1) + j2\pi f_1) + jK_{id} \\ b &= H_i(j2\pi(f_p + f_1) - j2\pi f_1) - jK_{id}. \end{aligned} \tag{12}$$

2) Circulating Current Control: The second circulating-current control loop only reacts to the common-mode components in the arm current among the three-phase arms, and thus the second circulating-current controller only works on current harmonics whose frequencies are $f = f_p + (6k \pm 2)f_1$, $k \in \mathrm{Z}$. Based on the abovementioned analysis, the coefficient matrix of the second circulating-current loop can be obtained by

$$\boldsymbol{Q}_c = \mathrm{diag}\,[0 \quad c \quad 0 \quad 0 \quad 0 \quad d \quad 0]. \tag{13}$$

In the coefficient matrix $\boldsymbol{Q}_c$, the frequency corresponding to coefficient c is $f_p - 2f_1$, which is the gain coefficient of positive-sequence component of the common mode, whereas

the frequency corresponding to coefficient *d* is $f_p + 2f_1$, which is the gain coefficient of negative-sequence component of the common mode.

The *dq*-decoupling-control-based PI controller is also used in the second circulating-current control loop, but different from the phase current control loop, the negative-sequence *dq* transformation will shift the frequency upward by $2f_1$ for positive-sequence harmonics and downward by $2f_1$ for negative-sequence harmonics. Based on the abovementioned analysis, the parameters in the coefficient matrix $\boldsymbol{Q}_c$ can be obtained

$$\begin{aligned} c &= H_c(j2\pi(f_p - 2f_1) + j4\pi f_1) + jK_{cd} \\ d &= H_c(j2\pi(f_p + 2f_1) - j4\pi f_1) - jK_{cd}. \end{aligned} \tag{14}$$

3) DC Voltage Control: The dc-side voltage perturbation is compensated by the dc voltage compensator and the phase current compensator and then added to the insertion index *m* after *dq* inverse transformation. In addition, the compensated dc-side voltage perturbation will generate two new small-signal harmonics after *dq* inverse transformation, and the amplitude and frequency will be different from before.

Assuming the compensated voltage perturbation is

$$\hat{m}_{dq} = \begin{bmatrix} M_d \cos(\theta_p + \varphi) \\ 0 \end{bmatrix}. \tag{15}$$

The harmonics after *dq* inverse transformation are shown as

$$\begin{aligned} \hat{m} &= T_{dq}^T \cdot \hat{m}_{dq} = \frac{1}{2} M_d \\ &\times \begin{bmatrix} \cos[(\theta_p - \theta) + \varphi] + \cos[(\theta_p + \theta) + \varphi] \\ \cos\left[(\theta_p - \theta) + \varphi + \frac{2\pi}{3}\right] + \cos\left[(\theta_p + \theta) + \varphi - \frac{2\pi}{3}\right] \\ \cos\left[(\theta_p - \theta) + \varphi - \frac{2\pi}{3}\right] + \cos\left[(\theta_p + \theta) + \varphi + \frac{2\pi}{3}\right] \end{bmatrix} \end{aligned} \tag{16}$$

where $\theta = 2\pi f_1 t$ and $\theta_p = 2\pi f_p t$.

According to the results after the *dq* inverse transformation, it can be found that the amplitudes of two small-signal harmonics are half of the original, and the frequencies are $f_p - f_1$ and $f_p + f_1$, respectively. Among them, the small-signal harmonic with frequency of $f_p - f_1$ is negative-sequence component among three phases, whereas the small-signal harmonic with frequency of $f_p + f_1$ is positive-sequence component among three phases. Therefore, the coefficient matrix $\boldsymbol{P}_v$ of the dc voltage control loop can be expressed as

$$\boldsymbol{P}_v(:, 4) = [0 \quad 0 \quad e \quad 0 \quad f \quad 0 \quad 0]^T. \tag{17}$$

The matrix $\boldsymbol{P}_v$ has zero elements in all columns except column 4. The frequency corresponding to coefficient *e* is $f_p - f_1$, whereas the frequency corresponding to coefficient *f* is $f_p + f_1$, but the frequency in compensator is f_p. Therefore, the coefficient in the matrix $\boldsymbol{P}_v$ can be obtained by

$$\begin{aligned} e &= H_v(j2\pi f_p) H_i(j2\pi f_p)/2 \\ f &= H_v(j2\pi f_p) H_i(j2\pi f_p)/2. \end{aligned} \tag{18}$$

4) Phase-Locked Loop: Fig. 4(a) shows the control block diagram of the PLL, and its small-signal model can be simplified as the control block diagram shown in Fig. 4(b) [23], [24].

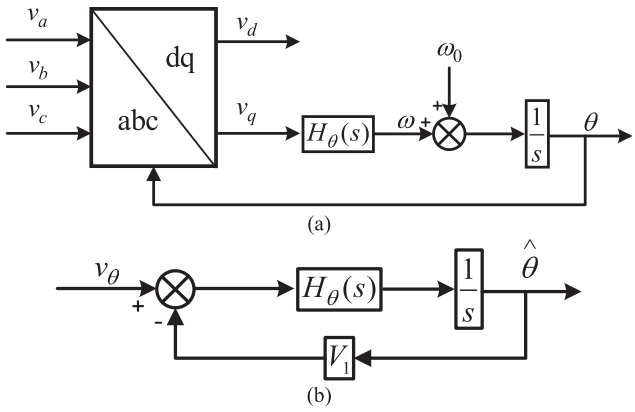

Fig. 4. (a) Block diagram of a basic PLL. (b) Its linearized model.

Analyzing the relationships of small-signal responses among three phases, when a voltage perturbation with frequency f_p is added to the dc side of MMC, the ac terminal will generate a positive-sequence voltage harmonic with frequency $f_p + f_1$ and a negative-sequence voltage harmonic with frequency $f_p - f_1$. These harmonics will perturb the output phase angle of the PLL and further affect the control system of MMC.

When the ac side contains a positive-sequence voltage harmonic ($f = f_p + f_1$), the output phase angle perturbation of the PLL can be obtained by

$$\hat{\theta} = -j\frac{V_s}{2} e^{j\varphi} \begin{bmatrix} 0 \\ 0 \\ 0 \\ G_\theta(j2\pi f_p) \\ 0 \\ 0 \\ 0 \end{bmatrix} \begin{matrix} \\ \\ \\ \leftarrow f_p \\ \\ \\ \end{matrix} \begin{matrix} \\ \\ \leftarrow f_p - f_1 \\ \\ \leftarrow f_p + f_1 \\ \\ \\ \end{matrix} \tag{19}$$

where V_s and φ are amplitude and phase of the ac voltage harmonic, respectively, and $G_\theta(s)$ is the closed-loop transfer function of PLL. It can be found that the frequency is shifted downward by f_1 when the ac side contains a positive-sequence voltage perturbation.

Based on the abovementioned analysis, the *dq* transformation matrix with phase angle perturbation can be obtained by

$$\begin{aligned} \boldsymbol{T}_{dq}(\theta + \hat{\theta}) &\approx \boldsymbol{T}_{dq}(\theta) + \hat{\theta}\frac{d}{\mathrm{d}t}\boldsymbol{T}_{dq}(\theta) \\ &= \boldsymbol{T}_{dq}(\theta) + \hat{\theta}\boldsymbol{T}_{dq}\left(\theta + \frac{\pi}{2}\right). \end{aligned} \tag{20}$$

And the *dq* inverse transformation matrix is

$$\boldsymbol{T}_{dq}^T(\theta + \hat{\theta}) \approx \boldsymbol{T}_{dq}^T(\theta) + \hat{\theta}\boldsymbol{T}_{dq}^T\left(\theta + \frac{\pi}{2}\right). \tag{21}$$

Therefore, this phase angle perturbation will affect all processes, including *dq* transformation and *dq* inverse transformation, respectively.

PLL dynamic effect should be considered both in dc voltage control loop and current control loop when MMC operates in the dc voltage control mode. Each phase current and dc voltage contain a steady state and a series of small-signal harmonics.

Similarly, each *dq*-frame compensator output also contains a steady state (dc) and a series of small-signal harmonics. The *dq*-frame current control models presented in Section III-A1 captured the small-signal response due to the multiplication of the first term on the right-hand side of (20) and (21) with the small-signal harmonics in phase currents and the *dq*-frame compensator outputs, respectively. The *dq*-frame dc voltage control model presented in Section III-A3 captured the small-signal response due to the multiplication of the first term on the right-hand side of (21) with small-signal harmonics in the *dq*-frame compensator outputs.

Multiplication of steady-state component of the phase currents with the second term of (20) leads to new small-signal harmonics. And these new small-signal harmonics will be propagated to insertion index through current controller and first term of (21). Multiplication of the second term of (21) with the steady-state component of the *dq*-frame compensator outputs leads to new small-signal harmonics. It should be noted that this process represents the PLL dynamic effect of both dc voltage control loop and current control loop, because the steady-state component of the *dq*-frame compensator outputs includes information of both dc voltage control loop and current control loop.

New small-signal harmonics from multiplication of steady-state component of the phase currents with the second term of (20) is analyzed as below.

Assuming the fundamental current of ac terminal is

$$\boldsymbol{i}_s = \begin{bmatrix} i_a \\ i_b \\ i_c \end{bmatrix} = \begin{bmatrix} I_1\cos(\theta+\varphi_z) \\ I_1\cos(\theta-\frac{2\pi}{3}+\varphi_z) \\ I_1\cos(\theta+\frac{2\pi}{3}+\varphi_z) \end{bmatrix}. \tag{22}$$

After *dq* transformation, the small-signal response to phase angle perturbation is

$$\hat{\theta}\cdot\boldsymbol{T}_{dq}\left(\theta+\frac{\pi}{2}\right)\cdot\boldsymbol{i}_s = \hat{\theta}\begin{bmatrix} I_1\cos(\varphi_z-\frac{\pi}{2}) \\ I_1\cos(\varphi_z-\pi) \end{bmatrix}. \tag{23}$$

After compensated by the phase current loop compensator and *dq* inverse transformation, this small-signal response further becomes

$$\boldsymbol{T}_{dq}^T(\theta+\hat{\theta})\cdot\begin{bmatrix} \hat{i}_d \\ \hat{i}_q \end{bmatrix} \approx \frac{1}{2}V_sI_1G_\theta(j2\pi f_p)[H_i(j2\pi f_p)-jK_{id}]$$

$$\begin{bmatrix} \cos(\theta_p-\theta w+\varphi-\varphi_z)-\cos(\theta_p+\theta+\varphi+\varphi_z) \\ \cos\left(\theta_p-\theta+\varphi-\varphi_z+\frac{2\pi}{3}\right)-\cos\left(\theta_p+\theta+\varphi+\varphi_z-\frac{2\pi}{3}\right) \\ \cos\left(\theta_p-\theta+\varphi-\varphi_z-\frac{2\pi}{3}\right)-\cos\left(\theta_p+\theta+\varphi+\varphi_z+\frac{2\pi}{3}\right) \end{bmatrix}. \tag{24}$$

It can be found that the phase current control loop generates additional small-signal responses due to phase angle perturbation. Then, the steady-state insertion index will also respond to the phase angle perturbation in the *dq* inverse transformation. In addition, the response of the circulating current control loop to the phase angle perturbation can be neglected because the circulating current in the arm has been suppressed under the steady-state condition.

Similarly, new small-signal harmonics from multiplication of the second term of (21) with the steady-state component of the *dq*-frame compensator outputs are analyzed as below.

Assume that the fundamental component of the insertion index before the *dq* inverse transformation is

$$\begin{bmatrix} M_d \\ M_q \end{bmatrix} = \begin{bmatrix} M_1\cos(\phi) \\ M_1\cos\left(\phi-\frac{\pi}{2}\right) \end{bmatrix}. \tag{25}$$

After the *dq* transformation, the small-signal responses to phase angle perturbation is

$$\hat{\theta}T_{dq}^T\left(\theta+\frac{\pi}{2}\right)\cdot\begin{bmatrix} M_d \\ M_q \end{bmatrix} = \frac{1}{2}V_sM_1G_\theta(j2\pi f_p)$$
$$\cdot\begin{bmatrix} \cos(\theta_p+\theta+\varphi+\phi)-\cos(\theta_p-\theta+\varphi-\phi) \\ \cos\left(\theta_p+\theta+\varphi+\phi-\frac{2\pi}{3}\right)-\cos\left(\theta_p-\theta+\varphi-\phi+\frac{2\pi}{3}\right) \\ \cos\left(\theta_p+\theta+\varphi+\phi+\frac{2\pi}{3}\right)-\cos\left(\theta_p-\theta+\varphi-\phi-\frac{2\pi}{3}\right) \end{bmatrix}. \tag{26}$$

Therefore, when there is a positive-sequence voltage harmonic with frequency of f_p+f_1 on the ac terminal, the small-signal responses of the control system caused by the phase angle perturbation is

$$\frac{1}{2}G_\theta(j2\pi f_p)[\boldsymbol{M}_1-\boldsymbol{I}_1[H_i(j2\pi f_p)-jK_{id}]]$$
$$\cdot V_s\cos(\theta_p+\theta+\varphi)+\frac{1}{2}G_\theta(\mathrm{j}2\pi f_p)$$
$$\cdot[\boldsymbol{I}_1^*[H_i(j2\pi f_p)-jK_{id}]-\boldsymbol{M}_1^*]V_s\cos(\theta_p-\theta+\varphi) \tag{27}$$

where

$$\boldsymbol{M}_1=\frac{M_1}{2}e^{j\phi},\quad \boldsymbol{M}_1^*=\frac{M_1}{2}e^{-j\phi}$$
$$\boldsymbol{I}_1=\frac{I_1}{2}e^{j\varphi_z},\quad \boldsymbol{I}_1^*=\frac{I_1}{2}e^{-j\varphi_z}. \tag{28}$$

Similarly, when the ac terminal contains a negative-sequence voltage harmonic ($f=f_p-f_1$), the small-signal responses of the control system caused by the phase angle perturbation can be obtained by

$$\frac{1}{2}G_\theta(j2\pi f_p)[\boldsymbol{M}_1^*-\boldsymbol{I}_1^*[H_i(j2\pi f_p)+jK_{id}]]$$
$$\cdot V_s\cos(\theta_p-\theta+\varphi)+\frac{1}{2}G_\theta(j2\pi f_p)$$
$$\times[\boldsymbol{I}_1[H_i(j2\pi f_p)+jK_{id}]-\boldsymbol{M}_1]V_s\cos(\theta_p+\theta+\varphi). \tag{29}$$

In addition, the relationship among small-signal voltage harmonics and small-signal current harmonics on the ac side can be expressed as

$$\hat{v}_a=\boldsymbol{Z}_a\hat{i}_a=2\,\boldsymbol{Z}_a\hat{i}_u \tag{30}$$

where the small-signal impedance (including line impedance and load impedance) on the ac side is

$$\boldsymbol{Z}_a=\mathrm{diag}\,[0\quad 0\quad z(f_p-f_1)\quad 0\quad z(f_p+f_1)\quad 0\quad 0]. \tag{31}$$

Synthesizing the abovementioned derivation process, the small-signal model of PLL can be obtained by

$$\hat{m}_u = \boldsymbol{P}_{\rm pll}\hat{v}_a = 2\boldsymbol{P}_{\rm pll}\boldsymbol{Z}_a\hat{i}_u \tag{32}$$

where

$$\boldsymbol{P}_{\rm pll} = \begin{bmatrix} 0_{2\times2} & & & 0_{2\times2} \\ & A & 0 & B \\ & 0 & 0 & 0 \\ & C & 0 & D \\ 0_{2\times2} & & & 0_{2\times2} \end{bmatrix}. \tag{33}$$

And the corresponding coefficients in the matrix are

$$\begin{aligned} A &= \frac{1}{2}G_\theta(j2\pi f_p)[\boldsymbol{M}_1^* - \boldsymbol{I}_1^*[H_i(j2\pi f_p) + jK_{id}]] \\ B &= \frac{1}{2}G_\theta(j2\pi f_p)[\boldsymbol{I}_1^*[H_i(j2\pi f_p) - jK_{id}] - \boldsymbol{M}_1^*] \\ C &= \frac{1}{2}G_\theta(j2\pi f_p)[\boldsymbol{I}_1[H_i(j2\pi f_p) + jK_{id}] - \boldsymbol{M}_1] \\ D &= \frac{1}{2}G_\theta(j2\pi f_p)[\boldsymbol{M}_1 - \boldsymbol{I}_1[H_i(j2\pi f_p) - {\rm j}K_{id}]]. \end{aligned} \tag{34}$$

5) DC-Side Impedance Model of DC Voltage Control Mode: Based on the abovementioned analysis, the control system small-signal model of the dc voltage control mode can be simplified as

$$\hat{m}_u = (\boldsymbol{Q}_i + \boldsymbol{Q}_c + 2\boldsymbol{P}_{\rm pll}\boldsymbol{Z}_a)\hat{i}_u + \boldsymbol{P}_v\hat{v}_p/2. \tag{35}$$

Defining that $\boldsymbol{Z}_c = \boldsymbol{Y}_c^{-1}$, $\boldsymbol{Y}_l = \boldsymbol{Z}_l^{-1}$, and $\boldsymbol{U}$ is unit matrix. And then, substituting (35) into (6) and (7), the following can be obtained:

$$\begin{aligned} &2[\boldsymbol{U} + \boldsymbol{Y}_l(\boldsymbol{M}_u\boldsymbol{Z}_c\boldsymbol{M}_u + 2\boldsymbol{Z}_a) + \boldsymbol{Y}_l(\boldsymbol{V}_u + \boldsymbol{M}_u\boldsymbol{Z}_c\boldsymbol{I}_u) \\ &\quad\times \boldsymbol{Q}_i + \boldsymbol{Q}_c + 2\boldsymbol{P}_{\rm pll}\boldsymbol{Z}_a)]\hat{i}_u \\ &\quad - \boldsymbol{Y}_l[\boldsymbol{U} + (\boldsymbol{V}_u + \boldsymbol{M}_u\boldsymbol{Z}_c\boldsymbol{I}_u)\boldsymbol{P}_v]\hat{v}_p = 0. \end{aligned} \tag{36}$$

Then, the relationship among the small-signal current response of the upper arm and the voltage perturbation on the dc side is

$$\begin{aligned} \boldsymbol{Y}_p &= \frac{\hat{i}_u}{\hat{v}_p/2} \\ &= [\boldsymbol{U} + \boldsymbol{Y}_l(\boldsymbol{M}_u\boldsymbol{Z}_c\boldsymbol{M}_u + 2\boldsymbol{Z}_a) + \boldsymbol{Y}_l(\boldsymbol{V}_u + \boldsymbol{M}_u\boldsymbol{Z}_c\boldsymbol{I}_u) \\ &\quad\cdot(\boldsymbol{Q}_i + \boldsymbol{Q}_c + 2\boldsymbol{P}_{\rm pll}\boldsymbol{Z}_a)]^{-1}\boldsymbol{Y}_l[\boldsymbol{U} + (\boldsymbol{V}_u + \boldsymbol{M}_u\boldsymbol{Z}_c\boldsymbol{I}_u)\boldsymbol{P}_v]. \end{aligned} \tag{37}$$

Because there is a symmetrically similar relationship among the three-phase six arms of MMC, the only need is to conduct impedance modeling for one arm, and then multiply a corresponding coefficient to obtain the impedance model on the dc side

$$Z_{\rm dc}(f_p) = \frac{\hat{v}_p}{\hat{i}_{\rm dc}} = \frac{2}{3Y_p(n+1,n+1)}. \tag{38}$$

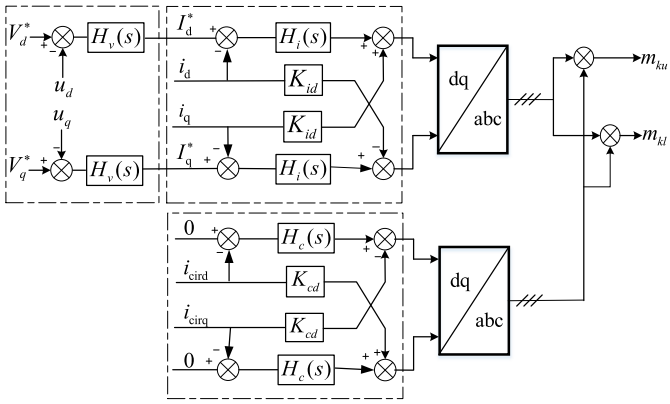

Fig. 5. Block diagram of the ac voltage control mode.

B. AC Voltage Control Mode

The MMC double-loop control block diagram of ac voltage control mode is shown in Fig. 5.

The frequency and phase angle of its ac voltage are fixed value, so the dynamics of the PLL can be ignored. And the small-signal model of the ac voltage control mode is equal to the superposition of the three control loops, which can be modeled by

$$\hat{m}_u = \boldsymbol{Q}_i\hat{i}_u + \boldsymbol{Q}_c\hat{i}_u + \boldsymbol{P}_a\hat{v}_a \tag{39}$$

where $\boldsymbol{Q}_i$, $\boldsymbol{Q}_c$, and $\boldsymbol{P}_a$ are the coefficient matrixes of the phase current control loop, the circulating current control loop, and the ac voltage control loop, respectively. In addition, the small-signal model of the phase current control loop and the circulating current control loop is the same as the dc voltage control mode, so it is unnecessary to elaborate.

1) Coupling of DC Impedance With AC-Side Network: The coefficient matrix of the ac voltage control can be obtained by

$$\boldsymbol{P}_a = {\rm diag}\,[0 \quad 0 \quad h \quad 0 \quad g \quad 0 \quad 0] \tag{40}$$

where the frequency corresponding to h in the coefficient matrix $\boldsymbol{P}_a$ is $f_p - f_1$, which is the gain coefficient of negative-sequence component of the differential mode, whereas the frequency corresponding to g is $f_p + f_1$, which is the gain coefficient of positive-sequence component of the differential mode. According to the previous analysis, *dq* transformation will shift the frequency downward by f_1 of positive-sequence harmonics and upward by f_1 for negative-sequence harmonics. In addition, the ac-side voltage perturbations are compensated by the ac voltage compensator and the phase current compensator, so the coefficient in the matrix $\boldsymbol{P}_a$ can be obtained by

$$\begin{aligned} g &= H_v(j2\pi f_p)H_i(j2\pi f_p)/2 \\ h &= H_v(j2\pi f_p)H_i(j2\pi f_p)/2. \end{aligned} \tag{41}$$

Therefore, in the modeling of the control system, the coupling relationship between the ac-side impedance and the dc-side impedance is reflected in the matrix. The different ac-side impedance will affect the small-signal model of the control system.

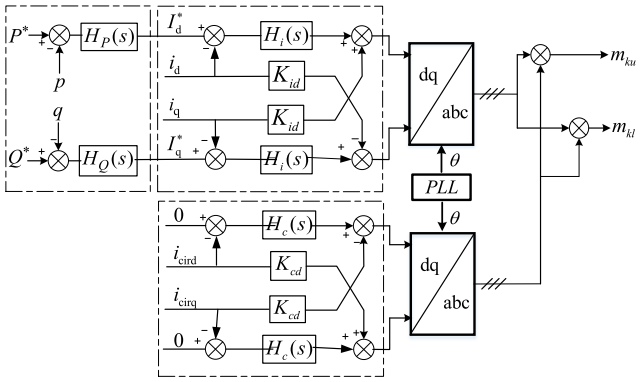

Fig. 6. Block diagram of the power control mode.

2) DC-Side Impedance Model of AC Voltage Control Mode: The control system small-signal model of the ac voltage control mode can be simplified as

$$\hat{m}_u = (\boldsymbol{Q}_i + \boldsymbol{Q}_c + 2\boldsymbol{P}_a\boldsymbol{Z}_a)\hat{i}_u. \tag{42}$$

And then, the relationship between the small-signal current response of upper arm and voltage perturbation on the dc side is

$$\boldsymbol{Y}_p = [\boldsymbol{U} + \boldsymbol{Y}_l(\boldsymbol{M}_u\boldsymbol{Z}_c\boldsymbol{M}_u + 2\boldsymbol{Z}_a) + \boldsymbol{Y}_l(\boldsymbol{V}_u + \boldsymbol{M}_u\boldsymbol{Z}_c\boldsymbol{I}_u) \times (\boldsymbol{Q}_i + \boldsymbol{Q}_c + 2\boldsymbol{P}_a\boldsymbol{Z}_a)]^{-1}\boldsymbol{Y}_l. \tag{43}$$

Substituting (43) into (38), the dc-side impedance model of ac voltage control mode can be obtained.

C. Power Control Mode

The MMC double-loop control block diagram of power control mode is shown in Fig. 6. It is equal to the superposition of the four control loops, so the small-signal model of power control mode can be modeled by

$$\hat{\boldsymbol{m}}_u = \boldsymbol{Q}_i\hat{i}_u + \boldsymbol{Q}_c\hat{i}_u + (\boldsymbol{M}\hat{p} + \boldsymbol{N}\hat{q}) + \boldsymbol{P}_{\mathrm{pll}}\hat{\boldsymbol{v}}_a \tag{44}$$

where $\boldsymbol{Q}_i$, $\boldsymbol{Q}_c$, $\boldsymbol{P}_{\mathrm{pll}}$, and ($\boldsymbol{M}$, $\boldsymbol{N}$) are the coefficient matrixes of the phase current control loop, the circulating current control loop, PLL, and the power control loop, respectively. In addition, the small-signal model of the phase current control loop and the circulating current control loop is the same as the dc voltage control mode, so it is unnecessary to elaborate.

1) Power Control: According to the instantaneous power theory, it can be obtained that

$$\begin{bmatrix} p \\ q \end{bmatrix} = 1.5\begin{bmatrix} u_d & u_q \\ u_q & -u_d \end{bmatrix}\begin{bmatrix} i_d \\ i_q \end{bmatrix} = \begin{bmatrix} 1.5u_di_d + 1.5u_qi_q \\ 1.5u_qi_d - 1.5u_di_q \end{bmatrix}. \tag{45}$$

Since the q-axis component of the fundamental steady-state ac terminal voltage is zero, the small-signal harmonics of active and reactive powers can be simplified as

$$\begin{aligned} \hat{p} &= 1.5(U_d\hat{i}_d + I_d\hat{u}_d + I_q\hat{u}_q) \\ &= 1.5[U_d + Z_aI_d - jZ_aI_q]\hat{i}_d \\ \hat{q} &= 1.5(I_d\hat{u}_q - U_d\hat{i}_q - I_q\hat{u}_d) \\ &= 1.5[-U_d + Z_aI_d - jZ_aI_q]\hat{i}_q \end{aligned} \tag{46}$$

where Z_a is the ac-side impedance. U_d is the d-axis current of three-phase ac voltage after dq transformation. I_d is the d-axis current. I_q is the q-axis current.

In order to establish the small-signal model of the power control loop, the small-signal model of each small-signal harmonic of active and reactive powers can be established respectively.

First of all, the small-signal model of the first small-signal harmonic of active power, which is $1.5U_d\hat{i}_d$, is established. When the ac terminal current contains a positive-sequence small-signal harmonic ($f = f_p + f_1$), the d-axis and the q-axis components of the small-signal harmonic are

$$\begin{aligned} \begin{bmatrix} \hat{i}_d \\ \hat{i}_q \\ \hat{i}_0 \end{bmatrix} &= T_{dq}\begin{bmatrix} \hat{i}_a \\ \hat{i}_b \\ \hat{i}_c \end{bmatrix} = T_{dq}\begin{bmatrix} i\cos(\theta_p + \theta_1 + \varphi_1) \\ i\cos(\theta_p + \theta_1 + 120^\circ + \varphi_1) \\ i\cos(\theta_p + \theta_1 - 120^\circ + \varphi_1) \end{bmatrix} \\ &= \begin{bmatrix} i\cos(\theta_p + \varphi_1) \\ i\cos\left(\theta_p - \frac{\pi}{2} + \varphi_1\right) \\ 0 \end{bmatrix} \end{aligned} \tag{47}$$

where $\theta = 2\pi f_1 t$ and $\theta_p = 2\pi f_p t$.

For the first component of small-signal harmonic ($1.5U_d\hat{i}_d$) of active power in (46), when compensated by the active power compensator and the phase current compensator, it can be expressed as

$$k_1\hat{i}_d = 1.5\,U_dH_P\,(j2\pi f_p)\,H_i\,(j2\pi f_p)\,\hat{i}_d. \tag{48}$$

After dq inverse transformation, it transfers to (49). As can be seen from (49), two small-signal harmonics after dq inverse transformation are generated. The frequencies are $f_p - f_1$ and $f_p + f_1$, respectively, and the gain of both small-signal harmonics is $k_1/2$ in

$$T_{dq}^T k_1\begin{bmatrix} \hat{i}_d \\ 0 \\ 0 \end{bmatrix} = \frac{k_1 i}{2} \times \begin{bmatrix} \cos(\theta_p - \theta_1 + \varphi_1) + \cos(\theta_p + \theta_1 + \varphi_1) \\ \cos(\theta_p - \theta_1 + 120^\circ + \varphi_1) + \cos(\theta_p + \theta_1 - 120^\circ + \varphi_1) \\ \cos(\theta_p - \theta_1 - 120^\circ + \varphi_1) + \cos(\theta_p + \theta_1 + 120^\circ + \varphi_1) \end{bmatrix}. \tag{49}$$

For the first component of small-signal harmonic ($-1.5U_d\hat{i}_q$) of reactive power in (46), when compensated by the reactive power compensator and the phase current compensator, it can be expressed as

$$k_2\hat{i}_q = -1.5U_dH_Q\,(j2\pi f_p)\,H_i\,(j2\pi f_p)\,\hat{i}_q. \tag{50}$$

Similar to the (49), after dq inverse transformation, it transfers to (51)

$$T_{dq}^T k_2\begin{bmatrix} 0 \\ \hat{i}_q \\ 0 \end{bmatrix} = \frac{k_2 i}{2} \times \begin{bmatrix} -\cos(\theta_p - \theta_1 + \varphi_1) + \cos(\theta_p + \theta_1 + \varphi_1) \\ -\cos(\theta_p - \theta_1 + 120^\circ + \varphi_1) + \cos(\theta_p + \theta_1 - 120^\circ + \varphi_1) \\ -\cos(\theta_p - \theta_1 - 120^\circ + \varphi_1) + \cos(\theta_p + \theta_1 + 120^\circ + \varphi_1) \end{bmatrix}. \tag{51}$$

Another case is that when the ac terminal current contains a negative-sequence small-signal harmonic ($f = f_p - f_1$), the d-axis and the q-axis components of the small-signal harmonic are

$$\begin{bmatrix} \hat{i}_d \\ \hat{i}_q \\ \hat{i}_0 \end{bmatrix} = T_{dq} \begin{bmatrix} \hat{i}_a \\ \hat{i}_b \\ \hat{i}_c \end{bmatrix} = T_{dq} \begin{bmatrix} i\cos(\theta_p - \theta_1 + \varphi_1) \\ i\cos(\theta_p - \theta_1 - 120^\circ + \varphi_1) \\ i\cos(\theta_p - \theta_1 + 120^\circ + \varphi_1) \end{bmatrix} = \begin{bmatrix} i\cos(\theta_p + \varphi_1) \\ i\cos\left(\theta_p + \frac{\pi}{2} + \varphi_1\right) \\ 0 \end{bmatrix}. \tag{52}$$

After the compensation and the dq inverse transformation, the first component of small-signal harmonic of active power and reactive power generates two small-signal harmonics of frequency $f_p - f_1$ and $f_p + f_1$

$$T_{dq}^T k_1 \begin{bmatrix} \hat{i}_d \\ 0 \\ 0 \end{bmatrix} = \frac{k_1 i}{2} \begin{bmatrix} \cos(\theta_p - \theta_1 + \varphi_1) + \cos(\theta_p + \theta_1 + \varphi_1) \\ \cos(\theta_p - \theta_1 + 120^\circ + \varphi_1) + \cos(\theta_p + \theta_1 - 120^\circ + \varphi_1) \\ \cos(\theta_p - \theta_1 - 120^\circ + \varphi_1) + \cos(\theta_p + \theta_1 + 120^\circ + \varphi_1) \end{bmatrix} \tag{53}$$

$$T_{dq}^T k_2 \begin{bmatrix} 0 \\ \hat{i}_q \\ 0 \end{bmatrix} = \frac{k_2 i}{2} \begin{bmatrix} \cos(\theta_p - \theta_1 + \varphi_1) - \cos(\theta_p + \theta_1 + \varphi_1) \\ \cos(\theta_p - \theta_1 + 120^\circ + \varphi_1) - \cos(\theta_p + \theta_1 - 120^\circ + \varphi_1) \\ \cos(\theta_p - \theta_1 - 120^\circ + \varphi_1) - \cos(\theta_p + \theta_1 + 120^\circ + \varphi_1) \end{bmatrix}. \tag{54}$$

Based on the abovementioned analysis, the small-signal model of the first component of small-signal harmonic of active power is

$$\hat{m}_d^1 = \frac{M}{2}\hat{i}_a = M\hat{i}_u = 3U_d P_{11}\hat{i}_u = 3U_d \begin{bmatrix} 0&0&0&0&0&0&0 \\ 0&0&0&0&0&0&0 \\ 0&0&m&0&m&0&0 \\ 0&0&0&0&0&0&0 \\ 0&0&m&0&m&0&0 \\ 0&0&0&0&0&0&0 \\ 0&0&0&0&0&0&0 \end{bmatrix} \begin{bmatrix} 0 \\ 0 \\ i\cos[2\pi(f_p - f_1) + \varphi_1]/2 \\ 0 \\ i\cos[2\pi(f_p + f_1) + \varphi_1]/2 \\ 0 \\ 0 \end{bmatrix} \tag{55}$$

where

$$m = H_P(j2\pi f_p)H_i(j2\pi f_p)/2. \tag{56}$$

Similarly, the small-signal model of the first component of small-signal harmonic of reactive power is

$$\hat{m}_q^1 = \frac{M}{2}\hat{i}_a = M\hat{i}_u = -3U_d P_{12}\hat{i}_u = -3U_d \times \begin{bmatrix} 0&0&0&0&0&0&0 \\ 0&0&0&0&0&0&0 \\ 0&0&n&0&-n&0&0 \\ 0&0&0&0&0&0&0 \\ 0&0&-n&0&n&0&0 \\ 0&0&0&0&0&0&0 \\ 0&0&0&0&0&0&0 \end{bmatrix} \begin{bmatrix} 0 \\ 0 \\ i\cos[2\pi(f_p - f_1) + \varphi_1]/2 \\ 0 \\ i\cos[2\pi(f_p + f_1) + \varphi_1]/2 \\ 0 \\ 0 \end{bmatrix} \tag{57}$$

where

$$n = H_Q(j2\pi f_p)H_i(j2\pi f_p)/2. \tag{58}$$

The small-signal models of the second component of small-signal harmonic of active power ($1.5Z_a I_d \hat{i}_d$) and reactive power ($1.5Z_a I_d \hat{i}_q$) are

$$\hat{m}_d^2 = \frac{M}{2}\hat{i}_a = M\hat{i}_u = 3Z_a I_d P_{21}\hat{i}_u = 3Z_a I_d \times \begin{bmatrix} 0&0&0&0&0&0&0 \\ 0&0&0&0&0&0&0 \\ 0&0&m&0&m&0&0 \\ 0&0&0&0&0&0&0 \\ 0&0&m&0&m&0&0 \\ 0&0&0&0&0&0&0 \\ 0&0&0&0&0&0&0 \end{bmatrix} \begin{bmatrix} 0 \\ 0 \\ i\cos[2\pi(f_p - f_1) + \varphi_1]/2 \\ 0 \\ i\cos[2\pi(f_p + f_1) + \varphi_1]/2 \\ 0 \\ 0 \end{bmatrix} \tag{59}$$

$$\hat{m}_q^2 = \frac{M}{2}\hat{i}_a = M\hat{i}_u = 3Z_a I_d P_{22}\hat{i}_u = 3Z_a I_d \times \begin{bmatrix} 0&0&0&0&0&0&0 \\ 0&0&0&0&0&0&0 \\ 0&0&n&0&-n&0&0 \\ 0&0&0&0&0&0&0 \\ 0&0&-n&0&n&0&0 \\ 0&0&0&0&0&0&0 \\ 0&0&0&0&0&0&0 \end{bmatrix} \begin{bmatrix} 0 \\ 0 \\ i\cos[2\pi(f_p - f_1) + \varphi_1]/2 \\ 0 \\ i\cos[2\pi(f_p + f_1) + \varphi_1]/2 \\ 0 \\ 0 \end{bmatrix}. \tag{60}$$

The small-signal models of the third component of small-signal harmonic of active power ($-j1.5Z_a I_q \hat{i}_d$) and reactive power ($-j1.5Z_a I_q \hat{i}_q$) are

$$\hat{m}_d^3 = \frac{M}{2}\hat{i}_a = M\hat{i}_u = 3Z_a I_q P_{31}\hat{i}_u = 3Z_a I_q \times \begin{bmatrix} 0&0&0&0&0&0&0 \\ 0&0&0&0&0&0&0 \\ 0&0&jm&0&-jm&0&0 \\ 0&0&0&0&0&0&0 \\ 0&0&jm&0&-jm&0&0 \\ 0&0&0&0&0&0&0 \\ 0&0&0&0&0&0&0 \end{bmatrix} \begin{bmatrix} 0 \\ 0 \\ i\cos[2\pi(f_p - f_1) + \varphi_1]/2 \\ 0 \\ i\cos[2\pi(f_p + f_1) + \varphi_1]/2 \\ 0 \\ 0 \end{bmatrix} \tag{61}$$

$$\hat{m}_q^3 = \frac{M}{2}\hat{i}_a = M\hat{i}_u = 3Z_aI_qP_{32}\hat{i}_u$$
$$= 3Z_aI_q \begin{bmatrix} 0 & 0 & 0 & 0 & 0 & 0 & 0 \\ 0 & 0 & 0 & 0 & 0 & 0 & 0 \\ 0 & 0 & jn & 0 & -j(-n) & 0 & 0 \\ 0 & 0 & 0 & 0 & 0 & 0 & 0 \\ 0 & 0 & j(-n) & 0 & -jn & 0 & 0 \\ 0 & 0 & 0 & 0 & 0 & 0 & 0 \\ 0 & 0 & 0 & 0 & 0 & 0 & 0 \end{bmatrix}$$
$$\times \begin{bmatrix} 0 \\ 0 \\ i\cos[2\pi(f_p - f_1) + \varphi_1]/2 \\ 0 \\ i\cos[2\pi(f_p + f_1) + \varphi_1]/2 \\ 0 \\ 0 \end{bmatrix}. \quad (62)$$

According to the abovementioned derivation method, the relationship among the other components in the active and reactive power harmonics and the insertion index can be deduced. Finally, the small-signal model of the power control loop can be modeled by

$$\begin{aligned}\hat{m}_u &= \hat{m}_d^1 + \hat{m}_q^1 + \hat{m}_d^2 + \hat{m}_q^2 + \hat{m}_d^3 + \hat{m}_q^3 \\ &= 3(U_dP_{11} + U_dP_{12} + Z_aI_dP_{21} + Z_aI_dP_{22} \\ &\quad + Z_aI_qP_{31} + Z_aI_qP_{32})\hat{i}_u \\ &= 3(U_dP_1 + Z_aI_dP_2 + Z_aI_qP_3)\hat{i}_u \end{aligned} \quad (63)$$

where I_d, I_q, and U_d are steady-state values of d-axis and q-axis components of ac terminal current and voltage, and the matrices $\boldsymbol{P}_1$, $\boldsymbol{P}_2$, and $\boldsymbol{P}_3$ are

$$\boldsymbol{P}_1 = \begin{bmatrix} 0 & 0 & 0 & 0 & 0 & 0 & 0 \\ 0 & 0 & 0 & 0 & 0 & 0 & 0 \\ 0 & 0 & m-n & 0 & m+n & 0 & 0 \\ 0 & 0 & 0 & 0 & 0 & 0 & 0 \\ 0 & 0 & m+n & 0 & m-n & 0 & 0 \\ 0 & 0 & 0 & 0 & 0 & 0 & 0 \\ 0 & 0 & 0 & 0 & 0 & 0 & 0 \end{bmatrix} \quad (64)$$

$$\boldsymbol{P}_2 = \begin{bmatrix} 0 & 0 & 0 & 0 & 0 & 0 & 0 \\ 0 & 0 & 0 & 0 & 0 & 0 & 0 \\ 0 & 0 & m+n & 0 & m-n & 0 & 0 \\ 0 & 0 & 0 & 0 & 0 & 0 & 0 \\ 0 & 0 & m-n & 0 & m+n & 0 & 0 \\ 0 & 0 & 0 & 0 & 0 & 0 & 0 \\ 0 & 0 & 0 & 0 & 0 & 0 & 0 \end{bmatrix} \quad (65)$$

$$\boldsymbol{P}_3 = \begin{bmatrix} 0 & 0 & 0 & 0 & 0 & 0 & 0 \\ 0 & 0 & 0 & 0 & 0 & 0 & 0 \\ 0 & 0 & j(m+n) & 0 & -j(m-n) & 0 & 0 \\ 0 & 0 & 0 & 0 & 0 & 0 & 0 \\ 0 & 0 & j(m-n) & 0 & -j(m+n) & 0 & 0 \\ 0 & 0 & 0 & 0 & 0 & 0 & 0 \\ 0 & 0 & 0 & 0 & 0 & 0 & 0 \end{bmatrix}. \quad (66)$$

The corresponding coefficients in the matrix are

$$\begin{aligned} m &= H_P(j2\pi f_p)H_i(j2\pi f_p)/2 \\ n &= H_Q(j2\pi f_p)H_i(j2\pi f_p)/2. \end{aligned} \quad (67)$$

2) Phase-Locked Loop: Except the fundamental ac terminal current and fundamental insertion index, the power control loop will also responses to the phase angle perturbation. Based on previous analysis, the fundamental phase current will produce two components after *dq* transformation, and the small-signal harmonic caused by the phase angle perturbation is

$$\hat{\theta}T_{dq}\left(\theta + \frac{\pi}{2}\right) \cdot i_s = \hat{\theta}\begin{bmatrix} i\cos\left(\varphi_z - \frac{\pi}{2}\right) \\ i\cos(\varphi_z - \pi) \end{bmatrix}. \quad (68)$$

So, the small-signal harmonic of power caused by the phase angle perturbation is

$$\begin{bmatrix} \hat{p} \\ \hat{q} \end{bmatrix} = 1.5U_d\begin{bmatrix} \hat{i}_d \\ -\hat{i}_q \end{bmatrix} = 1.5U_d\hat{\theta}\begin{bmatrix} i\cos\left(\varphi_z - \frac{\pi}{2}\right) \\ -i\cos(\varphi_z - \pi) \end{bmatrix}. \quad (69)$$

When there is a positive-sequence voltage harmonic in ac terminal ($f = f_\mathrm{p} + f_1$), this small-signal harmonic will generate two new small-signal responses after the compensation and the *dq* inverse transformation, which can be expressed as

$$\frac{3U_d}{4}V_siG_\theta(j2\pi f_p)H_P(j2\pi f_p)H_i(j2\pi f_p)$$
$$\cdot \begin{bmatrix} \cos(\theta_p+\theta+\varphi-\varphi_z) - \cos(\theta_p-\theta+\varphi+\varphi_z) \\ \cos(\theta_p+\theta+\varphi-\varphi_z-\frac{2\pi}{3}) - \cos\left(\theta_p-\theta+\varphi+\varphi_z+\frac{2\pi}{3}\right) \\ \cos(\theta_p+\theta+\varphi-\varphi_z+\frac{2\pi}{3}) - \cos\left(\theta_p-\theta+\varphi+\varphi_z-\frac{2\pi}{3}\right) \end{bmatrix}. \quad (70)$$

Similarly, when there is a negative-sequence voltage harmonic in the ac terminal ($f = f_p - f_1$), the final small-signal responses are

$$\frac{3U_d}{4}V_siG_\theta(j2\pi f_p)H_P(j2\pi f_p)H_i(j2\pi f_p)$$
$$\cdot \begin{bmatrix} \cos(\theta_p-\theta+\varphi+\varphi_z) - \cos(\theta_p+\theta+\varphi-\varphi_z) \\ \cos(\theta_p-\theta+\varphi+\varphi_z+\frac{2\pi}{3}) - \cos\left(\theta_p+\theta+\varphi-\varphi_z-\frac{2\pi}{3}\right) \\ \cos\left(\theta_p-\theta+\varphi+\varphi_z-\frac{2\pi}{3}\right) - \cos\left(\theta_p+\theta+\varphi-\varphi_z+\frac{2\pi}{3}\right) \end{bmatrix}. \quad (71)$$

So the small-signal model of PLL of the power control mode can be modeled by

$$\hat{m}_u = \boldsymbol{P}_\mathrm{pll}\hat{v}_a = 2\boldsymbol{P}_\mathrm{pll}\boldsymbol{Z}_a\hat{i}_u \quad (72)$$

where

$$\boldsymbol{P}_\mathrm{pll} = \begin{bmatrix} 0 & 0 & 0 & 0 & 0 & 0 & 0 \\ 0 & 0 & 0 & 0 & 0 & 0 & 0 \\ 0 & 0 & E & 0 & F & 0 & 0 \\ 0 & 0 & 0 & 0 & 0 & 0 & 0 \\ 0 & 0 & G & 0 & H & 0 & 0 \\ 0 & 0 & 0 & 0 & 0 & 0 & 0 \\ 0 & 0 & 0 & 0 & 0 & 0 & 0 \end{bmatrix} \quad (73)$$

$$E = A + 0.75U_d\boldsymbol{I}_1H_P(j2\pi f_p)H_i(j2\pi f_p)G_\theta(j2\pi f_p)$$
$$F = B - 0.75U_d\boldsymbol{I}_1H_P(j2\pi f_p)H_i(j2\pi f_p)G_\theta(j2\pi f_p)$$

TABLE I
ELECTRICAL PARAMETERS OF MMC

Control Mode	DC Voltage Control	AC Voltage Control	Power Control
Rated DC Voltage (kV)	500	500	500
Rated DC Power (MW)	750	750	1500
Rated AC Voltage (kV)	290	290	290
Submodule Capacitance (mF)	8	8	15
Number of Submodules/Arm	244	244	244
Rated DC Current (kA)	1.5	1.5	3
Arm Inductance (mH)	100	100	50
Arm Resistance (Ω)	0.3	0.3	0.3

$$G = C - 0.75U_d \boldsymbol{I}_1^* H_P(j2\pi f_p) H_i(j2\pi f_p) G_\theta(j2\pi f_p)$$
$$H = D + 0.75U_d \boldsymbol{I}_1^* H_P(j2\pi f_p) H_i(j2\pi f_p) G_\theta(j2\pi f_p). \tag{74}$$

3) DC-Side Impedance Model of Power Control Mode: Based on the abovementioned analysis, the control system small-signal model of the power control mode can be simplified as

$$\hat{m}_u = [\boldsymbol{Q}_i + \boldsymbol{Q}_c + 3(I_d \boldsymbol{P}_1 \boldsymbol{Z}_a + U_d \boldsymbol{P}_2 + I_q \boldsymbol{P}_3 \boldsymbol{Z}_a) + 2\boldsymbol{P}_{\text{pll}} \boldsymbol{Z}_a] \hat{i}_u. \tag{75}$$

And then, the relationship between the small-signal current response of the upper arm and the voltage perturbation on the dc side is

$$\boldsymbol{Y}_p = [\boldsymbol{U} + \boldsymbol{Y}_l(\boldsymbol{M}_u \boldsymbol{Z}_c \boldsymbol{M}_u + 2\boldsymbol{Z}_a) + \boldsymbol{Y}_l(\boldsymbol{V}_u + \boldsymbol{M}_u \boldsymbol{Z}_c \boldsymbol{I}_u) \cdot (\boldsymbol{Q}_i + \boldsymbol{Q}_c + 3(I_d \boldsymbol{P}_1 \boldsymbol{Z}_a + U_d \boldsymbol{P}_2 + I_q \boldsymbol{P}_3 \boldsymbol{Z}_a) + 2\boldsymbol{P}_{\text{pll}} \boldsymbol{Z}_a)]^{-1} \boldsymbol{Y}_l. \tag{76}$$

Substituting (76) into (38), the dc-side impedance model of power control mode can be obtained.

D. Impedance Model Verification

In order to verify the accuracy of the dc-side small-signal impedance model of MMC deduced in this article, a time-domain simulation model of MMC with three control modes was built based on MATLAB/Simulink. The main electrical parameters of MMC are shown in Table I. In addition, the modulation strategy of MMC adopts the nearest level approximation modulation, and the voltage balance control of submodule capacitor voltage adopts the sorting algorithm of submodule capacitor voltage. The corresponding control parameters are shown in Table II.

The simulation measurement of MMC dc-side impedance is based on the sweeping frequency method. A series of small signal voltage perturbations of different frequencies were added on the MMC dc side, and the small signal current response on the dc side of the corresponding frequency generated by the voltage disturbance was measured. Finally, the small-signal impedance on the MMC dc side at different frequencies was calculated. The analytical calculation of MMC dc-side impedance is based on the small-signal impedance modeling proposed above. After substituting the electrical parameters and control parameters of MMC into the established impedance model, we can obtain the dc-side impedance characteristic curve of MMC.

TABLE II
CONTROL PARAMETERS OF MMC

Control Loop	K_p	K_i	K_d
Phase Current Control	2.69×10^{-4}	3.59×10^{-3}	6.28×10^{-5}
Circulating Current Control	4×10^{-4}	4×10^{-3}	1.26×10^{-4}
DC Voltage Control	2.54×10^{-2}	1.06	N/A
AC Voltage Control	4.46×10^{-2}	7.13	N/A
Power Control	0.5	200	N/A
PLL	8.48×10^{-4}	0.015	N/A

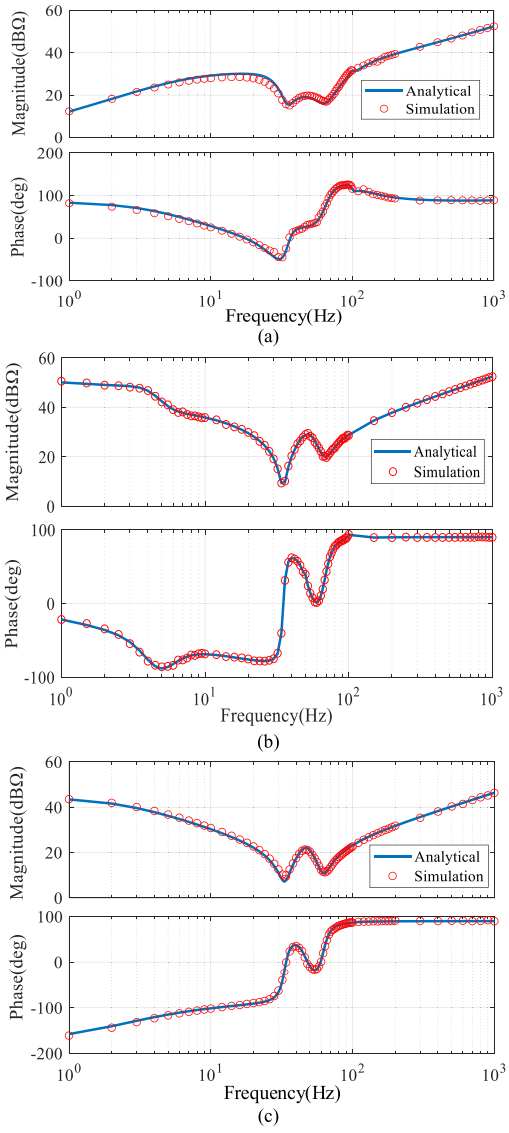

Fig. 7. Impedance responses with (a) dc voltage control mode, (b) ac voltage control mode, and (c) power control mode.

Fig. 7 shows the comparison of simulation and analytical of MMC dc-side impedance under the three control modes. Analytical results of impedance modeling are based on the third-order harmonic linearization approach. It can be seen from the figure that the analytical values under the three control modes match

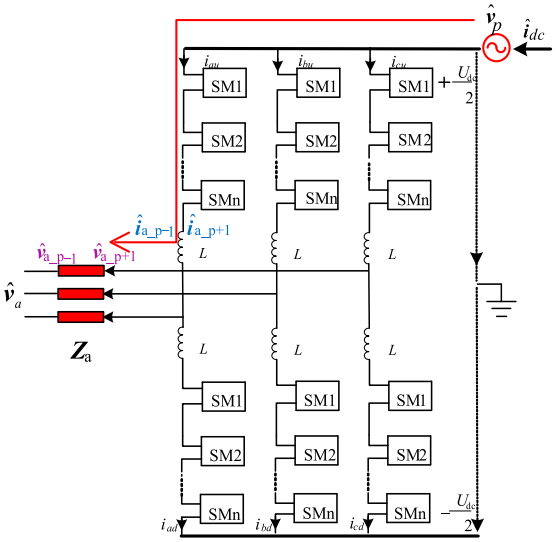

Fig. 8. Block diagram of the coupling process of the dc impedance with the ac-side network.

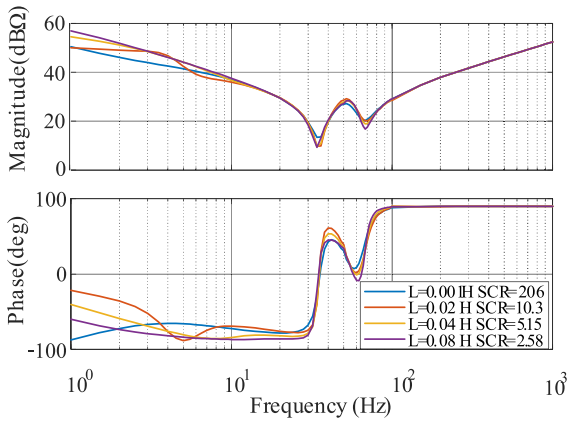

Fig. 9. Impact of ac-side network impedance on the dc-side impedance.

well with the simulation values, which proves the accuracy of the modeling method proposed in this article. Notably, as can be seen from the comparison of the three figures, the dc-side impedance of MMC under different control modes presents very different characteristics in the low-frequency band (below 30 Hz) due to the presence of external loop controller, so the small-signal model of outer control loop cannot be ignored. In addition, the dc-side impedance of MMC under power control mode presents negative-damping characteristic in the low-frequency band, which may affect the stability of its dc side.

E. Effect of the Grid Strength and Submodule Capacitor on Characteristics of DC Impedance

It is pointed out in [5] that ac-side network impedance will have effect on the middle- and low-frequency bands of dc impedance in two-level VSC. It makes a big difference to the accuracy of stability analysis with and without considering the coupling relationship of ac network and dc impedance of MMC.

Therefore, the following will introduce how the ac-side network impedance affects the dc-side impedance in the modeling process.

1) The process of coupling of the dc impedance of MMC with the ac-side network is shown in Fig. 8. When small disturbance voltage $\hat{v}_p$ of frequency f_p is added to the dc side of MMC, small-signal current response $\hat{i}_{\rm dc}$ will be produced on the ac side, as shown in Fig. 8.
2) Then, the small-signal arm current responses $\hat{i}_{a\_p-1}$ and $\hat{i}_{a\_p+1}$ of frequency $f_p \pm f_1$ will be generated on the ac side because of the coupling effect of MMC.
3) The small-signal currents $\hat{i}_{a\_p-1}$ and $\hat{i}_{a\_p+1}$ will generate the small disturbance voltages $\hat{v}_{a\_p-1}$ and $\hat{v}_{a\_p+1}$ on the ac-side impedance, which can be expressed as

$$\hat{v}_{a\_p-1} = 2Z_{ac(p-1)}\hat{i}_{a\_p-1} \tag{77}$$

$$\hat{v}_{a\_p+1} = 2Z_{ac(p+1)}\hat{i}_{a\_p+1}. \tag{78}$$

So, the small-signal disturbance voltage $\hat{v}_{a\_p-1}$ and $\hat{v}_{a\_p+1}$ caused by the ac-side network impedance will affect the electrical system small-signal model, which is shown in (6).

4) Therefore, the small-signal disturbance voltages $\hat{\boldsymbol{v}}_{a\_p-1}$ and $\hat{\boldsymbol{v}}_{a\_p+1}$ will generate small disturbance modulation wave responses $\hat{m}_{a\_p-1}$ and $\hat{m}_{a\_p+1}$ of frequency $f_p - f_1$ and $f_p + f_1$, respectively, through the PI controller of ac voltage control loop, inner current control loop, and *dq* inverse transformation, which can be expressed as

$$\begin{aligned}\hat{m}_{v\_p-1} &= H_v\left(j2\pi f_p\right) H_i\left(j2\pi f_p\right) \hat{v}_{a\_p-1}/2 \\ &= H_v\left(j2\pi f_p\right) H_i\left(j2\pi f_p\right) Z_{\mathrm{ac}(p-1)}\hat{i}_{a\_p-1}\end{aligned} \tag{79}$$

$$\begin{aligned}\hat{m}_{v\_p+1} &= H_v\left(j2\pi f_p\right) H_i\left(j2\pi f_p\right) \hat{v}_{a\_p+1}/2 \\ &= H_v\left(j2\pi f_p\right) H_i\left(j2\pi f_p\right) Z_{\mathrm{ac}(p+1)}\hat{i}_{a\_p+1}\end{aligned} \tag{80}$$

where $\boldsymbol{Z}_{\rm ac}$ is the ac-side impedance.

5) The ac network impedance will affect the dc impedance through the electrical system small-signal model and the control system small-signal model of MMC.

It is mentioned that the grid strength of the ac side will have effect on the dc impedance of MMC. Fig. 9 shows different dc-side impedance curves under the condition of different ac-side inductances, including 0.001 H (strong grid, SCR = 206), 0.02 H (SCR = 10.3), 0.04 H (SCR = 5.15), and 0.08 H (weak grid, SCR = 2.58). It is implied that different ac-side network impedances mainly affect the middle- (10–100 Hz) and low-frequency (1–10 Hz) bands of the dc-side impedance.

The submodule capacitor will also affect the characteristics of dc impedance. Taking the MMC under ac voltage control mode as an example, when the impedance at the ac side of MMC is 0.04 H, the changing trend of dc-side impedance of MMC is shown in Fig. 9 with the change of submodule capacitor from 4 to 240 mF.

The features shown in Fig. 10 can be concluded as follows.

1) The dc-side impedance of MMC tends to *LC* series impedance with the increase in submodule capacitor.
2) With the increase in the submodule capacitor, the resonance peak of the impedance curve will shift to the left,

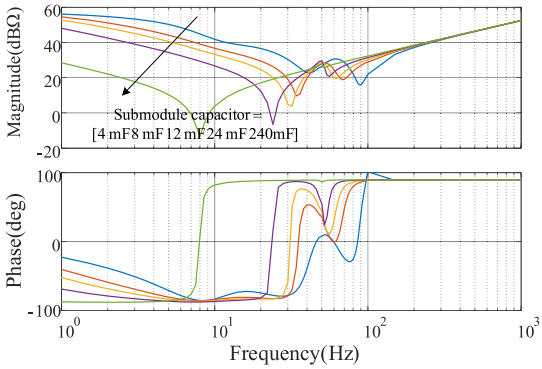

Fig. 10. DC-side impedance with different submodule capacitors.

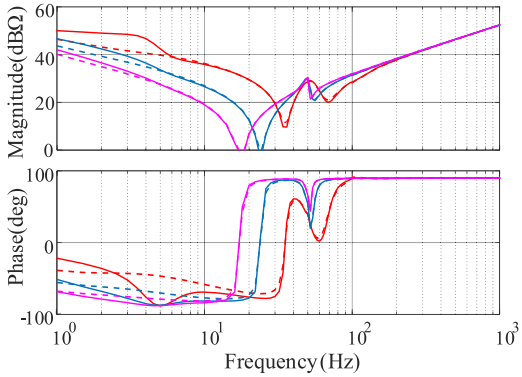

Fig. 11. Influence of the sizing of submodule capacitor on coupling of ac-side network and dc impedance (solid line and dotted line represent dc-side impedance curves of MMC with and without 0.02 H ac network impedance; the red, blue, and pink lines represent that submodule capacitor is 8 mF, 24 mf, and 48 mF, respectively).

and the resonant peak frequency of the impedance is about equal to

$$f_0 = \frac{1}{4\pi}\sqrt{\frac{N}{LC}}. \tag{81}$$

The size of submodule capacitor will also have effect on coupling of ac-side network and dc-side impedance. Along with the increase in submodule capacitance C, ac-side small-signal current response $\hat{i}_{a\_p-1}$ and $\hat{i}_{a\_p+1}$ generated by the coupling between dc-side voltage disturbance $\hat{v}_p$ and the fundamental frequency modulation wave will decrease. Then, the voltage drop on the ac-side impedance $\hat{v}_{a\_p-1}$ and $\hat{v}_{a\_p+1}$ of $\hat{v}_a$ in (6) will decrease so that the influence of ac network impedance on the MMC electrical system small-signal model will be reduced. At the same time, the effect of the ac-side small-signal current response $\hat{v}_{a\_p-1}$ and $\hat{v}_{a\_p+1}$ on MMC control system small-signal model will also be reduced.

Taking the MMC under ac voltage control mode as an example, the blue solid line and the blue dotted line represent the difference between dc impedance with and without 0.02 H ac-side network impedance when the submodule capacitor is 8 mF, the red solid and dotted lines represent that of difference when the submodule capacitor is 24 mF. And the pink solid line and the pink dotted line represent that of difference when the submodule capacitor is 48 mF.

According to Fig. 11, where $\boldsymbol{Z}_{\rm ac}$ represents ac side 0.02 H inductance, it indicates that the influence of ac-side inductance on dc impedance decreases with the increase in submodule capacitance. So the conclusion can be drawn that the effect of the coupling of the ac network with the dc impedance will decrease with the increase in submodule capacitor.

F. Influence of Different Orders of Harmonic Linearization on the Accuracy of Impedance Modeling

Fig. 12 shows comparison of simulation and analytical results of MMC dc-side impedance under different orders of harmonic linearization modeling.

The definition of the zeroth order of harmonic linearization modeling is that only the dc component of the submodule capacitor voltage and the component of frequency f_p in the control system small-signal model are considered. Similarly, the first order of harmonic linearization modeling means that

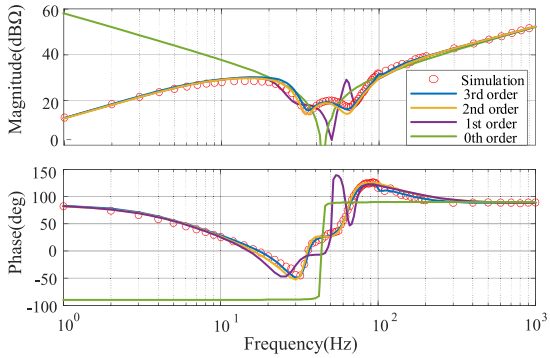

Fig. 12. Impedance responses using different orders of harmony line linearization approach.

the dc and fundamental components of the submodule capacitor voltage and the component including frequency f_p and $f_p \pm f_1$ in the control system small-signal model are considered.

Observing these curves, it can be inferred that the dc impedance curve considering the third-order modeling is basically consistent with the simulated result, and the dc impedance curves under the second- and the third-order of harmonic linearization modeling are slightly different. In addition, the dc impedance curve considering fundamental component has a large difference with the simulation result in the middle-frequency band (10–100 Hz). So, the dc impedance curve without considering any harmonic is not accurate.

The reason for the error under the zeroth-order modeling is that it ignores the fundamental component, the second component, and the third component of submodules capacitor voltage where fundamental component and the second component of submodule capacitor voltage are greater than 1% compared with the dc component of submodule capacitor voltage shown in Fig. 13. Ignoring the fundamental component and the second component of submodule capacitor voltage will lead to a large error.

At the same time, taking the phase current control loop and the second circulating-current control loop matrix that can be

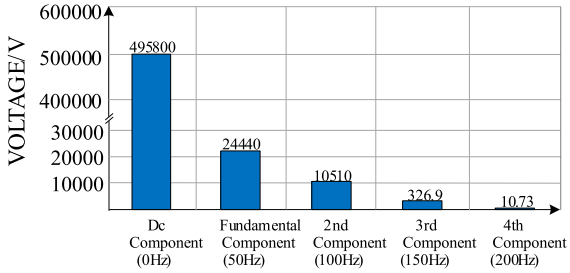

Fig. 13. Frequency distribution in sum of submodule capacitor voltages of per arm.

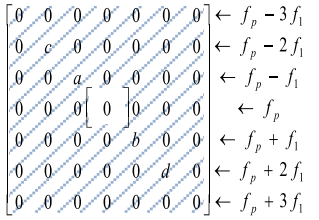

Fig. 14. Small-signal matrix of the current inner loop and the loop suppression loop with only zero-order accuracy.

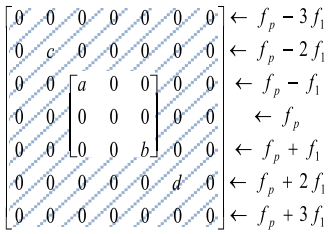

Fig. 15. Small signal matrix of the current inner loop and the loop suppression loop with only one-order accuracy.

expressed as $Q_i + Q_c$, as shown in Fig. 14, for the model without considering any harmonic, the matrix of small-signal model will only contain the component of frequency f_p. Elements representing frequency $f_p \pm f_1$, $f_p \pm 2f_1$, and $f_p \pm 3f_1$ in small-signal model will be ignored, and the matrix representing the control system small-signal model will become 1×1-order matrix, which means that *a*, *b*, *c,* and *d* in the matrix shown in Fig. 14 will be ignored.

Therefore, the dc impedance without considering any harmonic is not accurate.

Similarly, for the small-signal model only considering fundamental component, the matrix only contains the fundamental component of submodules capacitor voltage. The matrix of small-signal model will only contain the components of frequency f_p and $f_p \pm f_1$, so the elements in matrix of small-signal model representing frequency $f_p \pm 2f_1$ and $f_p \pm 3f_1$ will be ignored. The matrix representing the control system small-signal model will become second-order square matrix, which means that *c* and *d* in the matrix shown in Fig. 15 will be ignored.

Above all, if the *n*th components are less than 1% of the dc component of submodule capacitor voltages, and the elements on the *n*th order of control system small-signal matrix are zero, ignoring *n*th order components of model has no effect on the accuracy of the impedance modeling accuracy.

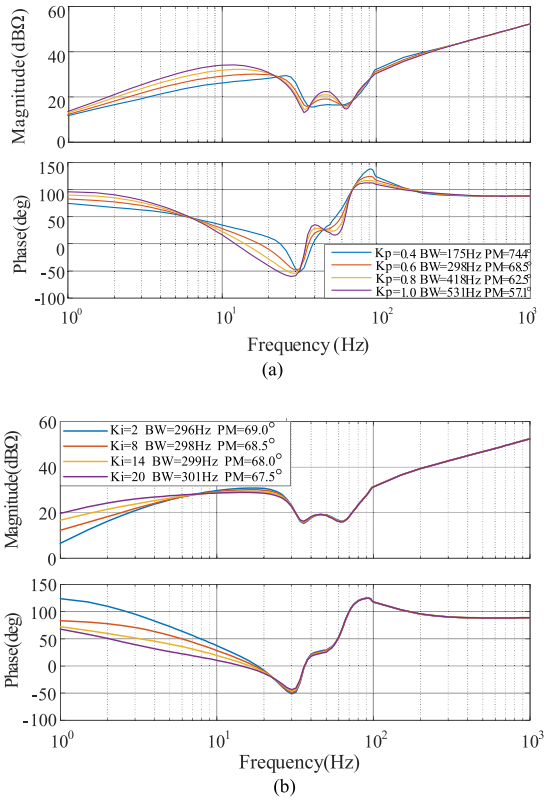

Fig. 16. Curves of dc impedance changing with the parameters of controllers in the dc voltage control mode. (a) K_p of current controller. (b) K_i of current controller.

G. Comparison of MMC DC-Side Impedance With Different Parameters of Controllers

Fig. 16 shows the comparison of MMC dc-side impedances obtained by different parameters of current inner loop under dc voltage control mode. The PI parameters of the current inner loop are initially set as $K_p = 0.6$ and $K_i = 8$. The corresponding bandwidth and phase margin are 300 Hz and 68.5°, respectively. The changes of impedance are compared with the variation of K_p and K_i, respectively. It can be seen from Fig. 16(a) that as K_p increases from 0.4 to 1.0, the bandwidth increases from 175 to 531 Hz, and the phase margin decreases from 74.4° to 57.1°. DC-side impedance magnitude increases whereas impedance phase fluctuates in the low- and middle-frequency bands. Moreover, it can be seen from Fig. 16(b) that as K_i increases from 2 to 20, the bandwidth increases from 296 to 301 Hz, and the phase margin decreases from 69.0° to 67.5°. DC-side impedance magnitude increases whereas impedance phase decreases in the low- and middle-frequency bands.

Fig. 17 shows the comparison of MMC dc-side impedances with different control parameters of the dc voltage controller. The PI parameter of the dc voltage controller is initially set as $K_p = 12$ and $K_i = 500$, and the corresponding bandwidth and phase margin are 33 Hz and 66.7°, respectively. The changes

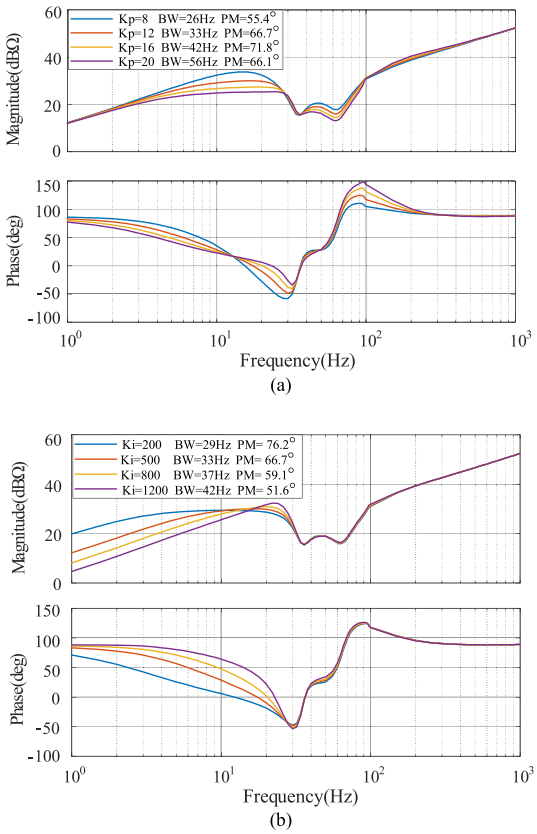

Fig. 17. Curves of dc impedance changing with the parameters of controllers in the dc voltage control mode. (a) K_p of the dc voltage controller. (b) K_i of the dc voltage controller.

of impedance are compared with the variation of K_p and K_i, respectively. It can be seen from Fig. 17(a) that as K_p increases from 8 to 20, the bandwidth increases from 26 to 56 Hz, and the phase margin first increases from 55.4° to 71.8° and then decreases to 66.1°. And impedance magnitude decreases whereas impedance phase fluctuates in the low- and middle-frequency band. Moreover, it can be seen from Fig. 17(b) that as K_i increases from 200 to 1200, the bandwidth increases from 29 to 42 Hz, and the phase margin decreases from 76.2° to 51.6°. DC-side impedance magnitude decreases whereas impedance phase increases in the low-frequency band.

In addition, the PI parameters of power controller, circulating current controller, and PLL have little effect on the MMC dc-side impedance, so no more figures in detail are shown here.

H. Comparison of MMC DC-Side Impedances Obtained by Different Modeling Methods

Fig. 18 shows the comparison of MMC dc-side impedances obtained by different modeling methods. The black line represents the impedance model obtained by the mean value modeling, the pink line represents the open-loop impedance model obtained by the harmonic linearization modeling, and the blue line represents the impedance model based on the impedance modeling method proposed in this article. It can be seen from the figure that the frequency impedance characteristics of these three models have a big difference below 100 Hz, which indicates

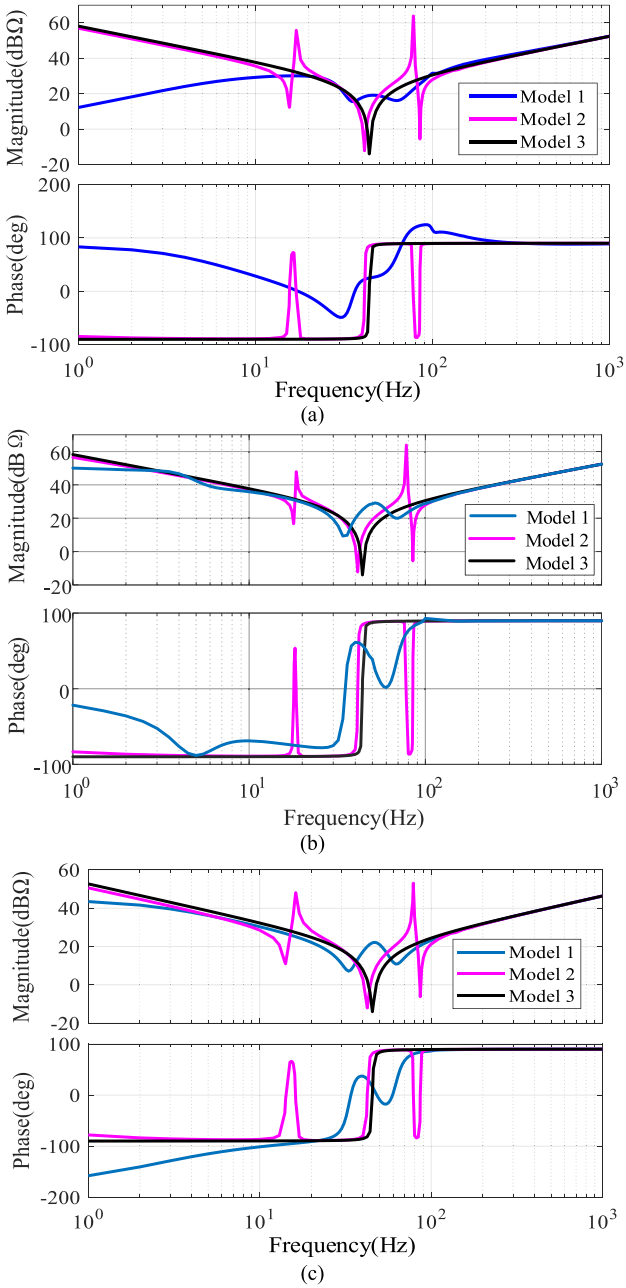

Fig. 18. Comparison of impedance with (a) dc voltage control mode, (b) ac voltage control mode, and (c) power control mode.

that the impedance model considering the influence of internal harmonic coupling characteristics and control system is very important for the accurate analysis of the low-frequency dc impedance characteristics of MMC.

IV. Stability Analysis of DC Ports in MMC-Based DC Grid

MMC-based dc grid is a complex system, and the stability of its dc system is the premise to ensure the stable operation of the whole system. Based on dc-side impedance modeling of MMC, the frequency impedance characteristics of the dc ports in the multiterminal MMC-based dc grid can be analyzed.

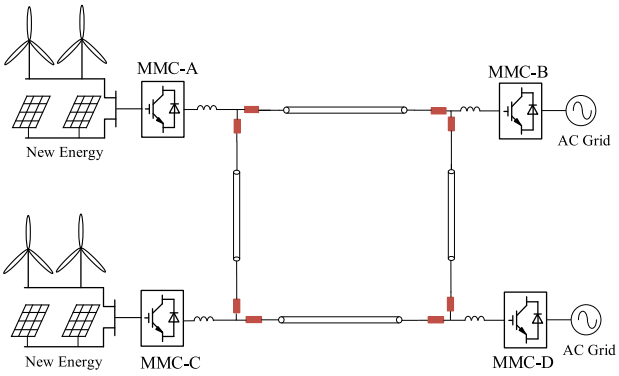

Fig. 19. Four-terminal MMC-based dc grid.

TABLE III
ELECTRICAL PARAMETERS OF CONVERTER IN MMC-BASED GRID

Parameter	MMC1	MMC2	MMC3	MMC4
Operating condition	Rectifier	Voltage Control	Rectifier	Power Control
Rated DC Voltage (kV)	500	500	500	500
Rated DC Power (MW)	750	750	1500	1500
Rated AC Voltage (kV)	290	290	290	290
Submodule Capacitance (mF)	8	8	15	15
Number of Submodules/Arm	244	244	244	244
Rated DC Voltage (kV)	1.5	1.5	3	3
Arm Inductance (mH)	100	100	50	50
Arm Resistance (Ω)	0.3	0.3	0.3	0.3
Line Wave Reactor (mH)	300	300	300	300
Neutral Wire Reactor(mH)	300	300	300	300

TABLE IV
DC LINE PARAMETERS OF MMC-BASED GRID

Parameter	A-C	A-B	B-D	C-D
Length(km)	49.6	206	189.6	207.6
Resistance (Ω/km)	0.0398	0.0398	0.0398	0.0398
Capacitance (uF/km)	0.4185	0.4185	0.4185	0.4185
Reactance (mH/km)	0.1122	0.1122	0.1122	0.1122

TABLE V
CONTROL PARAMETERS OF MMC-BASED GRID

Control loop	K_p	K_i	K_d
Phase Current	2.69×10^{-4}	3.59×10^{-3}	6.28×10^{-5}
Circulating Current	4×10^{-4}	4×10^{-3}	1.26×10^{-4}
MMC-A outer loop	4.46×10^{-2}	7.13	N/A
MMC-B outer loop	2.54×10^{-2}	1.06	N/A
MMC-C outer loop	4.46×10^{-2}	7.13	N/A
MMC-D outer loop	0.5	200	N/A
PLL	8.48×10^{-4}	0.015	N/A

Furthermore, stability of dc system can be studied based on the impedance-based stability criterion.

Fig. 19 shows a four-terminal MMC-based dc grid, which includes four converter stations, and the dc side is connected to a loop network. The detailed system parameters are shown in Tables III–V. In this project, converter stations A and C operate in ac voltage control, whose ac side is connected to island new energy electric field. Converter station B operates in dc voltage control mode, whereas converter station D operates in power

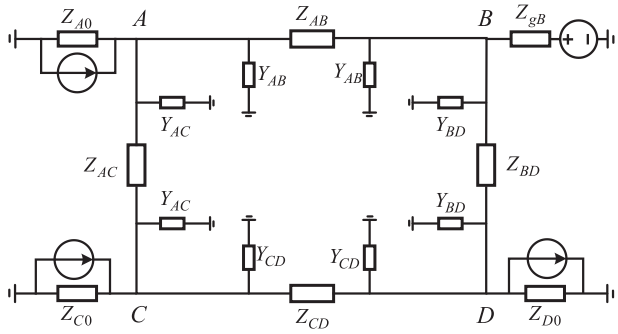

Fig. 20. Small-signal equivalent circuit of dc grid.

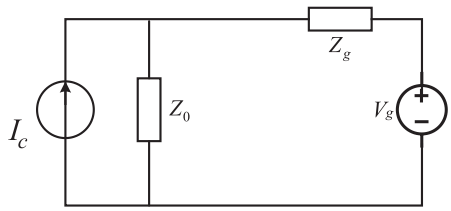

Fig. 21. Small-signal equivalent circuit of an interconnected system.

control. Converter station B and D ac side is connected to ac large power grid.

Based on MMC dc-side impedance modeling proposed in this article, the dc-side impedance model of these four converter stations can be obtained respectively. At the same time, the impedance of dc line can be obtained according to the circuit parameters presented in Table IV. Based on the aforementioned, the small-signal equivalent circuit of dc grid can be obtained, as shown in Fig. 20. According to the established small-signal equivalent circuit of dc grid, the stability of each dc port can be analyzed.

As shown in Fig. 21, each dc port in the MMC-based dc grid can be equivalent to the interconnection system of voltage source and current source according to Thevenin's theorem. And the small-signal impedance of dc grid can be obtained by circuit equivalence according to small-signal equivalent circuit of dc grid shown in Fig. 20. For each dc port, the side that supports the dc voltage is equivalent to one impedance in series of voltage source, whereas the other side is equivalent to one impedance in parallel of current source.

The power supply in Fig. 20 is set to zero. Taking port D as an example, the rest part of dc grid besides MMC D is equivalent to impedance Z_{gD}. The specific process is shown in Fig. 22.

Step 1: In Fig. 22(a), connect the impedance grounding terminals contained in the red dashed box.

Step 2: Combine the parallel impedance Z_{11}, Z_A, and Z_{21} in Fig. 22(a) into one impedance Z_{A1}, as shown in Fig. 22(b). Similarly, Z_{B1} and Z_{C1} can be obtained in the same way.

Step 3: Transform the impedances in Y connection (Z_{A1}, Z_1, and Z_2), as shown in the red dashed box in Fig. 22(b), into delta connection ($Z_{\triangle 11}$, $Z_{\triangle 12}$, $Z_{\triangle 13}$), as shown in Fig. 22(c), through the Y–$\triangle$ transformation.

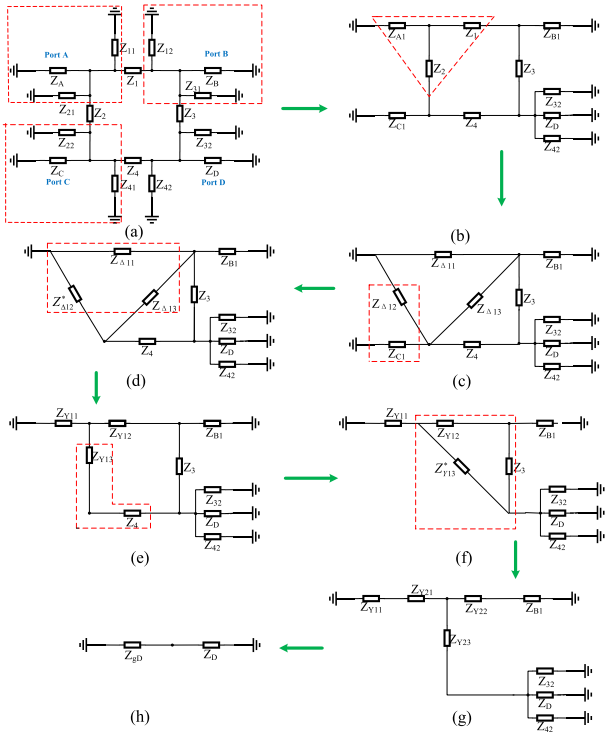

Fig. 22. Diagram of impedance network equivalent transformation.

Step 4: Combine $Z_{\triangle 12}$ and Z_{C1}, as shown in the red dashed box in Fig. 22(c), into one impedance $Z^*_{\Delta 12}$, as shown in Fig. 22(d).

Step 5: Transform the impedances in delta connection ($Z^*_{\Delta 12}, Z_{\Delta 11}, Z_{\Delta 13}$), as shown in the red dashed box n Fig. 22(d), into Y connection (Z_{Y11}, Z_{Y12}, Z_{Y13}) through △–Y transformation, as shown in Fig. 22(e).

Step 6: Combine Z_{Y13} and Z_4 into one impedance Z^*_{Y13} ($Z^*_{Y13} = Z_{Y13} + Z_4$), as shown in Fig. 22(f).

Step 7: Transform the impedances in delta connection ($Z^*_{Y13}, Z_{Y11}, Z_{Y12}$), as shown in the red dotted box in Fig. 22(f), into Y connection (Z_{Y21}, Z_{Y22}, Z_{Y23}) through △–Y transformation, as shown in Fig. 22(g).

Step 8: After a series of simple circuit transformations, Z_{gD} can be obtained, see Fig. 22(h).

According to the impedance-based stability criterions mentioned in [42]–[48], the stability of the interconnected system could be judged by checking whether the close-loop transfer function has right half plane (RHP) poles. Applying the Nyquist criterion or inverse Nyquist criterion depends on the number of RHP poles and RHP zeros of impedance ratio. If two subsystems has been proved to be stable, respectively, which means that there are no RHP poles in Z_g and $Z_0{}^{-1}$, the system stability could be judged by checking whether the Nyquist plot of impedance ratio $T_m(\mathrm{s}) = Z_g(s)/Z_0(s)$ encircles (–1, *j*0) point, where Z_g is the output impedance of voltage source subsystem and Z_0 is the output impedance of current source subsystem. It can also be stated as "The interconnected system is stable only when the amplitude of impedance Z_g is always less than impedance Z_0, or the phase margin at the intersection of amplitude curves of Z_g and Z_0 is greater than zero."

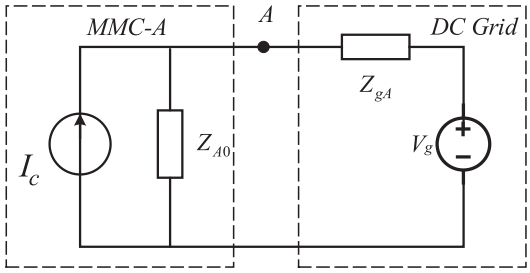

Fig. 23. Small-signal equivalent circuit of dc port A.

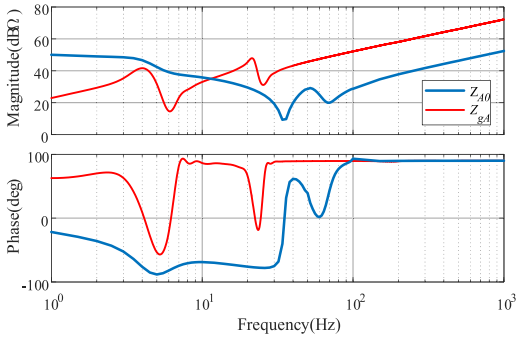

Fig. 24. Frequency impedance characteristics of dc port A.

If we apply the impedance ratio of $Z_0(s)/Z_g(s)$ to judge the port stability, inverse Nyquist criterion should be adopted, which is equivalent to applying the Nyquist criterion to the impedance ratio of $Z_g(s)/Z_0(s)$.

Based on the abovementioned analysis, here the impedance ratio of voltage source subsystem to current source subsystem is adopted to analyze the stability of ports A, B, C, and D. As for the four-port dc grid, as shown in Fig. 16, in order to analyze the stability of each dc port in the MMC-based dc grid, the dc grid need to be equivalent to an interconnection system consisting of a voltage source subsystem and a current source subsystem, as shown in Fig. 21, at ports A, B, C, and D respectively. In addition, before applying the Nyquist criterion at every dc port, the stability of subsystems has been verified, so the stability of these four ports could be evaluated by checking whether the number of the crossings in Bode plots of impedances is zero and calculating the phase margins [49].

A. *Frequency Impedance Characteristics of DC Port A*

For the dc port A, the dc grid supports the voltage for the dc side of converter station A, whereas the converter station A injects current into the dc grid as a current source. According to Thevenin's equivalence principle, dc port A can be equivalent to the circuit shown in Fig. 23. In the figure, Z_{A0} represents the dc-side impedance of converter station A, and Z_{gA} represents the small-signal equivalent impedance of dc grid at dc port A.

As shown in Fig. 24, the blue line is the Bode diagram of $Z_{A0}(s)$, whereas the red line represents the Bode diagram of $Z_{gA}(s)$.

When frequency tends to infinity, difference of the magnitude of impedance values $20\lg(|Z_{gA}|) - 20\lg(|Z_{A0}|)$ is a constant

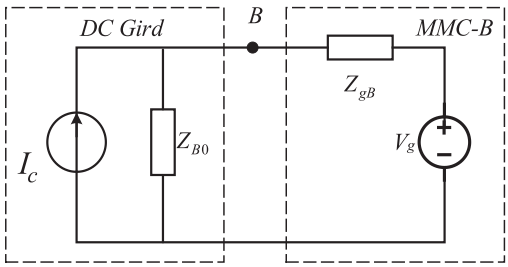

Fig. 25. Small-signal equivalent circuit of dc port B.

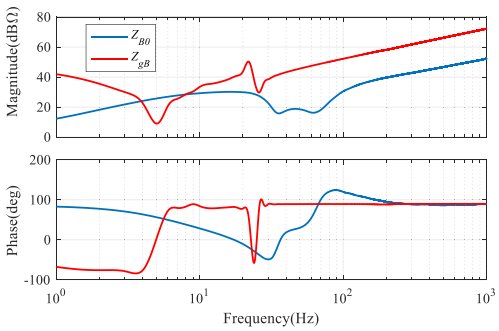

Fig. 26. Frequency impedance characteristics of dc port B.

value, which means the magnitude of the impedance ratio $|Z_{gA}|/|Z_{A0}|$ is a constant. Besides, the phase difference of Z_{gA} and Z_{A0} tends to 0. So the Nyquist plot of impedance ratio Z_{gA}/Z_{A0} will go to concentrate around the (k, 0) point, where k is a finite constant value. Therefore, the characteristics of impedance in high-frequency (1000–∞ Hz) band have no effect on the judgement of system stability. Instead, the system stability can be judged by applying Nyquist criterion in low-frequency (1–1000 kHz) band of frequency impedance curves. Similar conditions exist in station B, C, and D, which will not be explained repeatedly later. As for the impedance curves of dc port A in Fig. 24, it can be seen that the intersection frequency of amplitude curves of $Z_{A0}(s)$ and $Z_{gA}(s)$ is 10.2 Hz, and the phase margin is 27°, and thus dc port A is stable.

B. Frequency Impedance Characteristics of DC Port B

For dc port B, converter station B operates in dc voltage control mode, and its dc side supports the voltage of dc grid, whereas the dc grid inject power into converter station B. According to the principle of Thevenin's equivalence, dc port B can be equivalent to the circuit, as shown in Fig. 25. In the figure, Z_{gB} represents the dc-side impedance of converter station B, and Z_{B0} represents the small-signal equivalent impedance of the dc grid at dc port B.

The Bode diagram of $Z_{B0}(s)$ and $Z_{gB}(s)$ is shown in Fig. 26. It can found that the amplitude curves of $Z_{B0}(s)$ and $Z_{gB}(s)$ exist four intersections. According to the impedance-based stability criterion, the frequency of the intersection with minimum phase margin is 3.9 Hz, and the corresponding phase margin is 28°, so dc port B is stable.

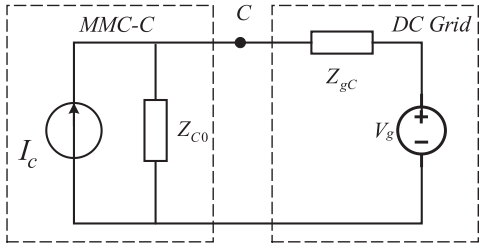

Fig. 27. Small-signal equivalent circuit of dc port C.

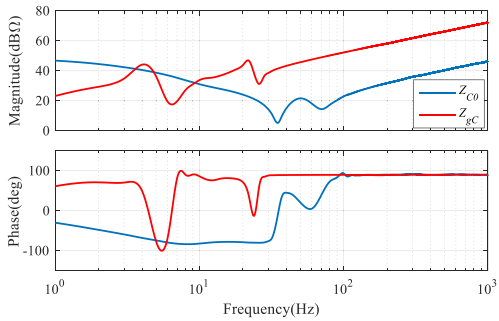

Fig. 28. Frequency impedance characteristics of dc port C.

C. Frequency Impedance Characteristics of DC Port C

For dc port C, the dc grid provides voltage support for the dc side of converter station C, whereas the converter station C injects dc current into the dc grid. According to the principle of Thevenin's equivalence, dc port C can be equivalent to the circuit, as shown in Fig. 27. In the figure, Z_{C0} represents the dc-side impedance of converter station C, and Z_{gC} represents the small-signal equivalent impedance of dc grid at dc port C.

The Bode diagram of $Z_{C0}(s)$ and $Z_{gC}(s)$ is shown in Fig. 28. It can be seen from the diagram that the amplitude curves of $Z_{C0}(s)$ and $Z_{gC}(s)$ exist three intersections. According to the impedance-based stability criterion, the frequency of the intersection with minimum phase margin is 9.5 Hz, and the corresponding phase margin is 13.5°, so dc port C is stable.

D. Frequency Impedance Characteristics of DC Port D

For dc port D, the dc grid provides voltage support for the dc side of converter station D, whereas the dc side of converter station D absorbs power from the dc grid. According to the principle of Thevenin's equivalence, dc port D can be equivalent to the circuit, as shown in Fig. 29. In the figure, Z_{D0} represents the dc-side impedance of converter station D, and Z_{gD} represents the small-signal equivalent impedance of dc grid at dc port D.

The Bode diagram of $Z_{D0}(s)$ and $Z_{gD}(s)$ is shown in Fig. 30. It can be seen from the diagram that the intersection frequency of amplitude curves of $Z_{D0}(s)$ and $Z_{gD}(s)$ is 9.3 Hz and the phase margin is 4°. It is obvious that the phase margin of dc port D is too small. Therefore, it is extremely easy for the system to oscillate and even collapse when the system operation conditions changed greatly. This is mainly because converter

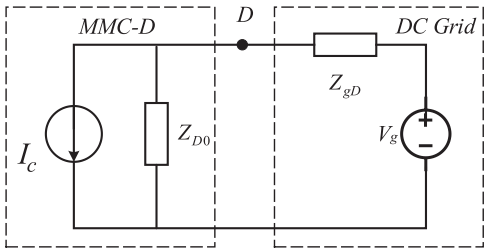

Fig. 29. Small-signal equivalent circuit of dc port D.

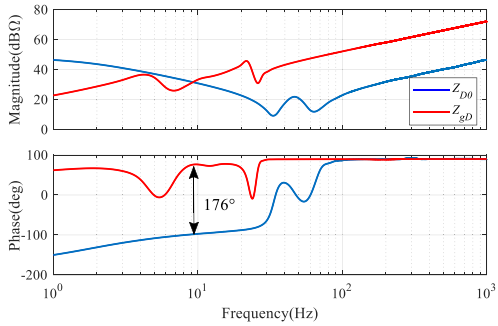

Fig. 30. Frequency impedance characteristics of dc port D.

station D adopts constant power control mode, and its dc-side impedance $Z_{D0}(s)$ shows negative impedance characteristics in the low-frequency band. Therefore, it is necessary to change the frequency impedance characteristic of $Z_{D0}(s)$ at the intersection to increase the phase margin of dc port D.

E. Verification of Stability Analysis

In order to verify the validity of stability analysis, a time-domain simulation of four-terminal MMC-based dc grid is built based on MATLAB/Simulink. The system parameters of the simulation model are consistent with those shown in Tables III–V. When the MMC-based dc grid is in a stable operation, make the transmission power of converter station under power control mode change and observe the change of operation characteristics of the whole dc system, as shown in Fig. 31.

Fig. 31 shows the current waveform on the dc side of the four converter stations when no stabilization measures are taken. As shown in Fig. 31(d), at 5 s, the transmission power of converter station D under power control mode jumps from 2/3 to 1 p.u. The dc-side current of converter station under power control mode shows a trend of divergent oscillation, and the magnitude of dc-side current increases very fast. The frequency of oscillation current is about 9 Hz, corresponding to the frequency at the intersection of $Z_{D0}(s)$ and $Z_{gD}(s)$ amplitude curves, which indicates the correctness of the stability analysis results. In addition, the dc-side current of other converter stations also oscillates to different degrees. By observing the current oscillation waveform of the four converter stations, it can be found that the oscillation current of dc port D flows into other dc ports through the dc line and causes current oscillation of other dc ports, in which dc port C is the most affected.

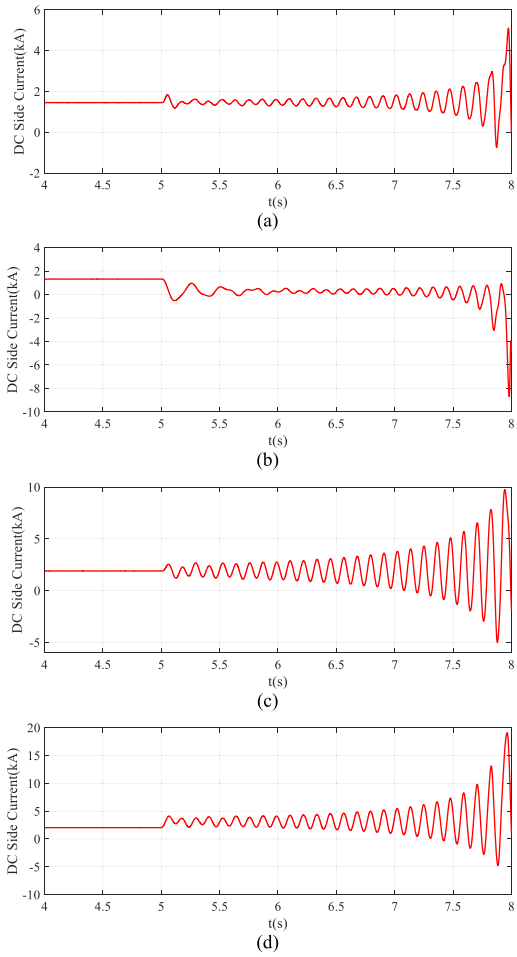

Fig. 31. DC-side current of four converter stations.

V. Control Strategy for Improving the Stability of the DC System

The dc-side impedance of converter station under power control mode shows negative-impedance characteristics in the low-frequency band, which makes its dc port prone to oscillation and other unstable problems. Therefore, in order to improve the stability of the dc system in the MMC-based dc grid, the dc-side frequency impedance characteristics of converter station under power control mode should be changed. In this article, the control strategy of optimizing controller parameters and adding virtual damping controller are adopted to improve the stability of dc system.

A. Optimization of Controller Parameters at Converter Station Under Power Control Mode

In view of the problem of insufficient phase margin of dc port D mentioned above, optimizing its controller parameters is the most effective improvement measure. Since the dc-side frequency impedance characteristics of MMC in low-frequency band are largely affected by the outer-loop controller parameters, it is supposed to keep the parameters of the inner-loop controller of converter station D unchanged and optimize the outer-loop

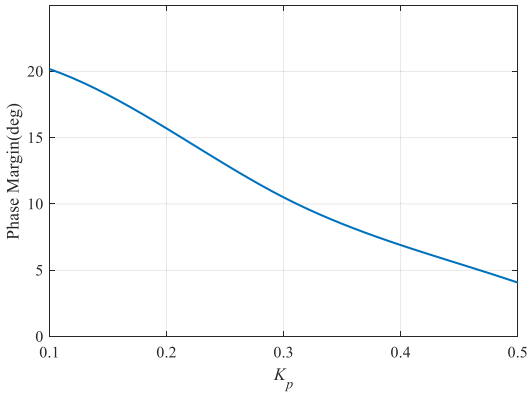

Fig. 32. Phase margin of dc port D varies with K_p.

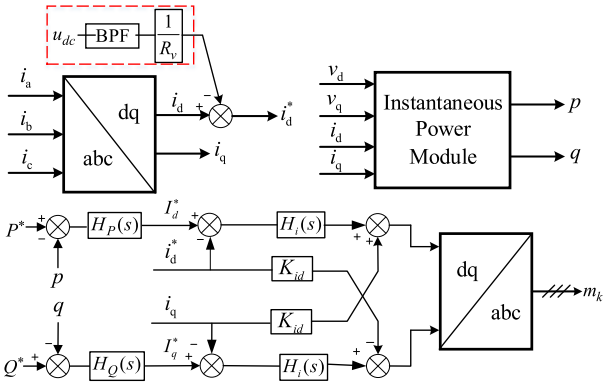

Fig. 33. Control block of converter station D with parallel damping controller.

controller parameters only. Meanwhile, in the optimization process, the ratio of proportional coefficient and integral coefficient of the outer loop should be kept at $K_i/K_p = 400$ to offset the main poles of the MMC closed-loop system. According to the engineering design experience, in order to ensure the MMC has a fast-dynamic response, the bandwidth of the outer-loop controller is generally designed to be no less than 1/10 of the inner-loop bandwidth, and the power outer-loop proportional coefficient K_p should be no less than 0.1 through calculation. At the same time, from the perspective of improving the phase margin of dc port D, the power outer-loop proportional coefficient K_p should not be greater than 0.5. Therefore, K_p ranges from 0.1 to 0.5.

As shown in Fig. 32, the phase margin of dc port D varies with K_p. As can be seen from the figure, the phase margin of dc port D gradually decreases as K_p changes from 0.1 to 0.5. However, the K_p is larger, the bandwidth of the outer-loop controller is higher, and the dynamic response speed of converter station D will be faster. Obviously, the tradeoff between the optimization of phase margin and dynamic response speed must be considered. In addition, the phase margin can reach 30° only when K_p is close to 0.1. However, if K_p is 0.1, the dynamic response speed of converter station D is slow, which is not conducive to the system timely response to dynamics. Therefore, considering improvement of both the dynamic characteristics and the phase margin of the system, K_p should be a compromise. In this article, K_p is selected as 0.2. As can be seen from Fig. 32, when K_p is 0.2, the phase margin of dc port D is 16°, and the phase margin is still insufficient. Therefore, it is necessary to furtherly improve the phase margin by adopting additional virtual damping control strategy.

B. Additional Virtual Parallel Damping Controller at Converter Station Under Power Control Mode

In the MMC-based dc grid mentioned in this article, the ac side of converter station D is connected to the strong ac grid, so it can be approximately considered that the ac-side voltage of converter station D remains unchanged, and the active power perturbation of dc port D can be simplified as

$$\Delta p = U_{\rm dc}\Delta i_{\rm dc} + I_{\rm dc}\Delta u_{\rm dc} = 1.5U_d\Delta i_d. \tag{82}$$

Assuming that the active power perturbation of dc port D is still Δp after parallel virtual resistance r_v, the active power perturbation flows into the converter station D dc port and changes to

$$\Delta p^* = \Delta p - U_{\rm dc}\frac{\Delta u_{\rm dc}}{r_v} = 1.5U_d\Delta i_d - U_{\rm dc}\frac{\Delta u_{\rm dc}}{r_v}. \tag{83}$$

For high-voltage and high-capacity MMC, the control system generally adopts the per unit value parameter. So after transforming (83) into per-unit values, it can be obtain by

$$\Delta P^* = \Delta I_d - \frac{\Delta U_{\rm dc}}{R_v} \tag{84}$$

where ΔP^*, ΔI_d, $\Delta U_{\rm dc}$, and R_v are per-unit values.

Based on the abovementioned analysis, if additional virtual parallel resistance controller is adopted, only one loop should be added to the original control structure of converter station D, as shown in the red box of Fig. 33. BPF is the bandpass filter, and its central frequency is the frequency of the intersection of Z_{D0} and Z_{gD} magnitude curves. In this article, it is set as 10 Hz, and the bandwidth is set as 8 Hz.

The value of virtual parallel resistance plays a decisive role in improving the phase margin of dc port D, so it is necessary to design the optimal value interval through detailed calculation. In the industry field, it is universally agreed that the phase margin of interconnected system is supposed to be designed as 30° to 60°. Thus, in this article, the phase margin is designed as 45°, and the parameter design of the parallel virtual damping controller will follow the abovementioned design criteria.

First, the outer-loop controller parameter of converter station D remain unchanged ($K_p = 0.2$, $K_i = 80$), and then the influence of the value of additional parallel virtual resistance on the phase margin of port D is studied. As shown in Fig. 34, the phase margin of dc port D varies with the value of the parallel virtual resistance. When the resistance value in parallel is getting smaller, the phase margin at the intersection of Z_{D0} and Z_{gD} amplitude curves will be larger. However, when the resistance value of the parallel resistor is getting smaller, the amplitude of Z_{D0} will be smaller, which will reduce the frequency of the intersection of Z_{D0} and Z_{gD} amplitude curves. This will make the designed bandpass filter have a high phase shift, and

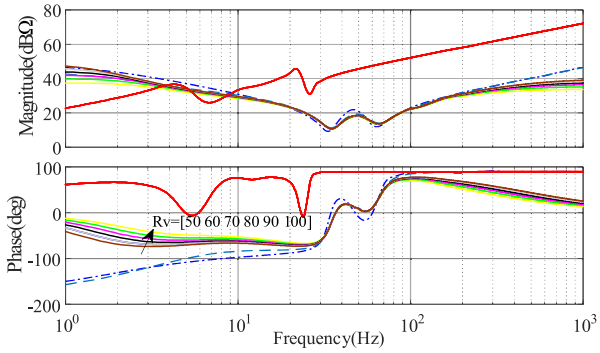

Fig. 34. Frequency impedance characteristics of dc port D varies with R_v and PI parameters.

the dynamic characteristics of the system will become worse. In fact, from both the perspective of the system dynamic and the damping characteristics of dc ports, the value of parallel resistance should not be too small. Therefore, in the guarantee intersection of Z_{D0} and Z_{gD}, amplitude curve under the premise of the phase margin is greater than 45°, and parallel virtual resistance value should be smaller to get bigger phase margin. It can be seen from Fig. 24, the phase margin of 45° corresponds to the parallel resistance whose value is 81.5 Ω. Therefore, parallel virtual resistance should be less than 81.5 Ω. In this article, the final parallel virtual resistance is 80 Ω, and the corresponding phase margin of dc port D is 46.5°.

According to Fig. 34, the influence process of the abovementioned two measures on the phase margin of station D is as follows.

1) By optimizing PI parameters, the phase–frequency curve of station D is shifted from blue dotted line to blue dashed line. By optimizing PI parameters, the phase margin is increased by 12°.
2) The phase margin is further increased by 30.5° by applying a virtual resistance of 80 Ω to increase damping at station D.

In addition, the impact of the abovementioned two measurements on the stability of other dc ports also needs to be considered. Calculation results shows that the phase margin of dc port A has been increased from 27° to 29°. The phase margin of dc port B has been increased from 28° to 92°, and the phase margin of dc port C has been increased from 13.5° to 29.7°. Obviously, the stability margin of the whole dc system is improved. Therefore, the abovementioned two measures can not only improve the phase margin of port D, but also effectively improve the stability of the whole system.

C. Verification of Control Strategy

The stabilization control strategy proposed in this article is applied to the converter station D to verify its validity. When the MMC-based dc grid is in stable operation, the transmission power of converter station D is changed, and the operating characteristics of the whole dc system are observed. The dc-side current waveforms of the four converter stations with stabilization control strategy are shown in Fig. 35.

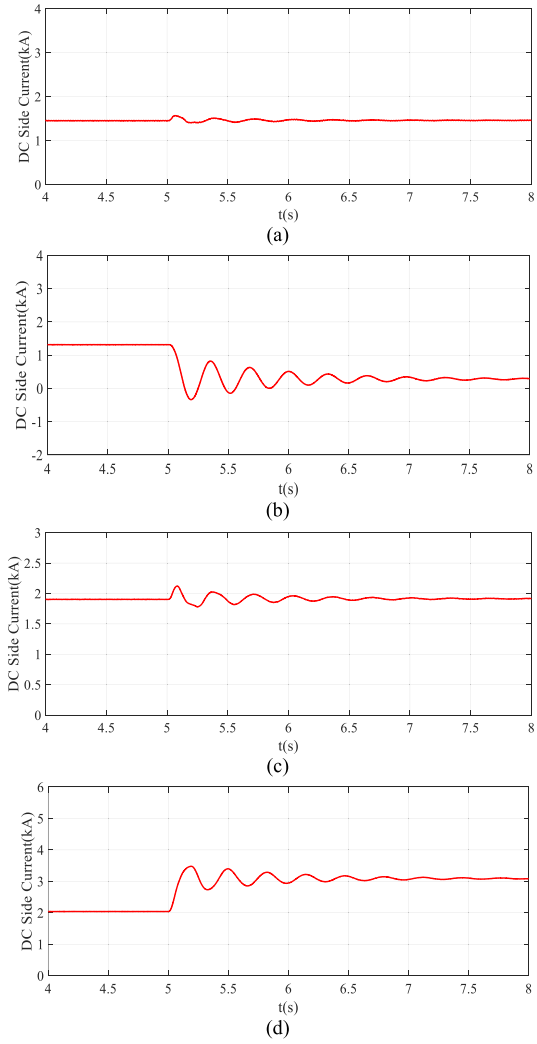

Fig. 35. DC-side current of four converter stations.

As can be seen from Fig. 35(d), at 5 s, the transmission power of the converter station D jumps from 2/3 to 1 p.u., the dc-side current reaches steady state after 2.5 s, and the overshoot of current is also small. This indicates that the stability of port D is greatly improved after adopting the two stabilization strategies mentioned above. In addition, comparing Figs. 31 and 35, it can be found that the oscillation current of other dc ports is also suppressed after the stabilization strategies are taken, which indicates that the stability of the whole system has been improved, verifying the validity of the stabilization strategy proposed in this article.

D. Comparison With Existing Control Strategies

In this section, the stabilization control strategy proposed in this article will be compared with two existing methods [50]. First, these two methods will be introduced briefly as follows.

Method 1 (dc voltage control mode with filter): In order to eliminate negative damping, which is caused by dc voltage control loop, a filter is added to the voltage outer loop in the dc voltage control. In this article, station B adopts dc voltage

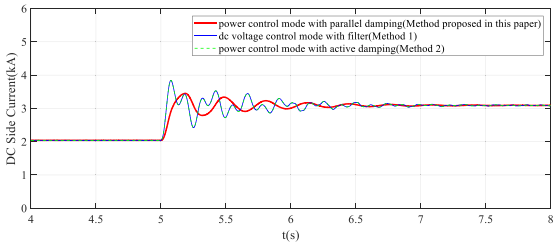

Fig. 36. DC-side current of D converter station under different improvement strategies.

control mode. After adding the filter, the dc voltage outer-loop transfer function of station B is

$$H_v^F(s) = \frac{k_p \cdot \omega_f}{s + \omega_f} + \frac{k_i}{s} \tag{85}$$

where k_p is proportionality coefficient in the PI controller, ω_f is the natural frequency of the low-pass filter, and k_i is integral coefficient in the PI controller.

Method 2 (power control mode with active damping): The active damping control can improve the harmonic stability of the system by adding compensating damping voltage to the insertion index of the bridge arm.

Fig. 36 shows the comparison of this article's improvement strategy with method 1 and method 2. As can be seen from Fig. 36, at 5 s, the transmission power of the converter station D jumps from 2/3 to 1 p.u. The red line has a smaller overshoot and reaches steady state much faster compared with the blue line and green line. Therefore, the method proposed in this article has better effect on the improvement of system stability.

VI. Conclusion

This article developed a dc-side impedance model of MMC. This impedance model considers the coupling characteristics of multiple harmonics within MMC and the complete small-signal model of control system under different control modes, making the small-signal impedance model established more accurate than previous researches. Meanwhile, it is found that the dc-side impedance of MMC presents different characteristics under different control modes. The main difference exists in low-frequency band due to the low bandwidth of the outer-loop controller.

Based on the presented impedance model, the stability of dc system in the MMC-based dc grid is analyzed according to impedance-based stability criterion. Since the dc-side impedance of converter station under power control mode shows negative impedance characteristics in low-frequency band, its dc port is prone to introduce oscillation and other unstable problems. Therefore, the control strategies such as optimizing controller parameters and adding virtual damping controller can be adopted to improve the stability of the dc system in MMC-based dc grid. Due to the high accuracy of impedance model presented in this article, the design of control strategy can meet the requirements of dynamic performance and stability. In this article, a bandpass filter is used to design the virtual damping controller, which can effectively improve the stability of the dc system and reduce the negative influence on the dynamic performance of the system.

References

[1] S. Dehnath, J. Qin, B. Bahrani, M. Saeedifard, and P. Barbosa, "Operation, control, and applications of the modular multilevel converter: A review," *IEEE Trans. Power Electron.*, vol. 30, no. 1, pp. 37–53, Jan. 2015.

[2] M. A. Perez, S. Bernet, J. Rodriguez, S. Kouro, and R. Lizana, "Circuit topologies, modeling, control schemes, and applications of modular multilevel converter," *IEEE Trans. Power Electron.*, vol. 30, no. 1, pp. 4–17, Jan. 2015.

[3] M. Amin and M. Molinas, "Small-signal stability assessment of power electronics based power systems: A discussion of impedance- and eigenvalue-based methods," *IEEE Trans. Ind Appl.*, vol. 53, no. 5, pp. 5014–5030, Sep./Oct. 2017.

[4] M. Amin, A. Rygg, and M. Molinas, "Impedance-based and eigenvalue based stability assessment compared in VSC-HVDC system," in *Proc. IEEE Energy Convers. Congr. Expo.*, Milwaukee, WI, USA, 2016, pp. 1–8.

[5] S. Shah and L. Parsa, "Impedance modeling of three-phase voltage source converters in DQ, sequence, and phasor domains," *IEEE Trans. Energy Convers.*, vol. 32, no. 3, pp. 1139–1150, Sep. 2017.

[6] L. Xu, L. Fan, and Z. Miao, "DC impedance-model-based resonance analysis of a VSCHVDC system," *IEEE Trans. Power Del.*, vol. 30, no. 3, pp. 1221–1230, Jun. 2015.

[7] M. Amin, M. Molinas, J. Lyu, and X. Cai, "Impact of power flow direction on the stability of VSC-HVDC seen from the impedance Nyquist plot," *IEEE Trans. Power Electron.*, vol. 32, no. 10, pp. 8204–8217, Oct. 2017.

[8] M. Amin and M. Molinas, "Impedance based stability analysis of VSC based HVDC system," in *Proc. IEEE Eindhoven PowerTech*, Eindhoven, The Netherlands, 2015, pp. 1–6.

[9] D. Xue, J. Liu, and Z. Liu, "DC terminal impedance model of voltage source converter with DC voltage control," in *Proc. IEEE Int. Power Electron. Appl. Conf. Expo.*, Shenzhen, China, 2018, pp. 1–4.

[10] J. Sun, "Impedance-based stability criterion for grid connected inverters," *IEEE Trans. Power Electron. Lett.*, vol. 26, no. 11, pp. 3075–3078, Nov. 2011.

[11] X. Zhang, X. Ruan, and C. K. Tse, "Impedance-based stability criterion for DC distributed power systems," *IEEE Trans. Circuits Syst.*, vol. 62, no. 3, pp. 916–925, Mar. 2015.

[12] B. Wen, D. Dong, D. Boroyevich, R. Burgos, P. Mattavelli, and Z. Shen, "Impedance-based analysis of grid-synchronization stability for three phase paralleled converters," *IEEE Trans. Power Electron.*, vol. 31, no. 1, pp. 26–38, Jan. 2016.

[13] M. A. Perez, S. Bernet, J. Rodriguez, S. Kouro, and R. Lizana, "Circuit topologies, modeling, control schemes, and applications of modular multilevel converter," *IEEE Trans. Power Electron.*, vol. 30, no. 1, pp. 4–17, Jan. 2015.

[14] L. Harnefors, A. Antonopoulos, S. Norrga, L. Angquist, and H. P. Nee, "Dynamic analysis of modular multilevel converters," *IEEE Trans. Ind. Electron.*, vol. 60, no. 7, pp. 2526–2537, Jul. 2013.

[15] K. Ilves, A. Antonopoulos, S. Norrga, and H. P. Nee, "Steady-state analysis of interaction between harmonic components of arm and line quantities of modular multilevel converters," *IEEE Trans. Power Electron.*, vol. 27, no. 1, pp. 57–68, Jan. 2012.

[16] X. Li, Q. Song, W. Liu, S. Xu, Z. Zhu, and X. Li, "Performance analysis and optimization of circulating current control for modular multilevel converter," *IEEE Trans. Ind. Electron.*, vol. 63, no. 2, pp. 716–727, Feb. 2016.

[17] D. Ludois and G. Venkataramanan, "Simplified terminal behavioral model for a modular multilevel converter," *IEEE Trans. Power Electron.*, vol. 29, no. 4, pp. 1622–1631, Apr. 2014.

[18] G. Bergna, J. A. Suul, and S. D'Arco, "Small-signal state-space modeling of modular multilevel converters for system stability analysis," in *Proc. IEEE Energy Convers. Congr. Expo.*, 2015, pp. 5822–5829.

[19] N. T. Trinh, M. Zeller, K. Wuerflinger, and I. Erlich, "Generic model of MMC-VSC-HVDC for interaction study with ac power system," *IEEE Trans. Power Syst.*, vol. 31, no. 1, pp. 27–34, Jan. 2016.

[20] X. Shi, Z. Wang, B. Liu, Y. Li, L. M. Tolbert, and F. Wang, "DC impedance modeling of a MMC-HVDC system for dc voltage ripple prediction under a single-line-to-ground fault," in *Proc. IEEE Energy Convers. Congr. Expo.*, Pittsburgh, PA, USA, 2014, pp. 5339–5346.

[21] R. Mo, Q. Ye, and H. Li, "DC impedance modeling and stability analysis of modular multilevel converter for MVDC application," in *Proc. IEEE Energy Convers. Congr. Expo.*, Milwaukee, WI, USA, 2016, pp. 1–5.
[22] D. Xu, M. Han, and A. M. Gole, "Propagation of AC background harmonics in MMC HVDC multiterminal systems due to resonances and mitigation measures," *IEEE Trans. Power Del.*, vol. 33, no. 1, pp. 229–238, Feb. 2018.
[23] J. Sun and H. Liu, "Sequence impedance modeling of modular multilevel converters," *IEEE J. Emerg. Sel. Topics Power Electron.*, vol. 5, no. 4, pp. 1427–1442, Dec. 2017.
[24] L. Xiong, X. Liu, C. Zhao, and F. Zhuo, "A fast and robust real-time detection algorithm of decaying DC transient and harmonic components in three-phase systems, " *IEEE Trans. Power Electron.*, vol. 35, no. 4, pp. 3332–3336, Apr. 2020.
[25] J. Lyu, X. Zhang, X. Cai, and M. Molinas, "Harmonic state-space based small-signal impedance modeling of modular multilevel converter with consideration of internal harmonic dynamics," *IEEE Trans. Power Electron.*, vol. 34, no. 3, pp. 2134–2148, Mar. 2019.
[26] H. Wu, X. Wang, and Ł. Kocewiak, "Impedance-based stability analysis of voltage-controlled MMCs feeding linear AC systems," *IEEE J. Emerg. Sel. Topics Power Electron.*, to be published, doi: 10.1109/JESTPE.2019.2911654.
[27] Z. Xu, B. Li, S. Wang, S. Zhang, and D. Xu, "Generalized single-phase harmonic state space modeling of the modular multilevel converter with zero-sequence voltage compensation," *IEEE Trans. Ind. Electron.*, vol. 66, no. 8, pp. 6416–6426, Aug. 2019.
[28] J. Lyu, X. Zhang, Z. Ma, and X. Cai, "A novel DC-side-port impedance modeling of modular multilevel converters based on harmonic state space method," in *Proc. IPEC-Niigata -ECCE Asia*, Niigata, Japan, 2018, pp. 4162–4167.
[29] W. Wu *et al.*, "A virtual phase-lead impedance stability control strategy for the maritime VSC–HVDC system," *IEEE Trans. Ind. Informat.*, vol. 14, no. 12, pp. 5475–5486, Dec. 2018.
[30] Y. Li *et al.*, "Modeling and damping control of modular multilevel converter based dc grid," *IEEE Trans. Power Syst.*, vol. 33, no. 1, pp. 723–735, Jan. 2018.
[31] H. Wu and X. Wang, "Dynamic impact of zero-sequence circulating current on modular multilevel converters: Complex valued AC impedance modeling and analysis," *IEEE J. Emerg. Sel. Topics Power Electron.*, to be published, doi: 10.1109/JESTPE.2019.2951446.
[32] N. Ahmed, L. Ängquist, S. Norrga, A. Antonopoulos, L. Harnefors, and H.-P. Nee, "A computationally efficient continuous model for the modular multilevel converter," *IEEE J. Emerg. Sel. Topics Power Electron.*, vol. 2, no. 4, pp. 1139–1148, Dec. 2014.
[33] J. Sun and H. Chao, "Impedance modeling and analysis of modular multilevel converters," in *Proc. IEEE 17th Workshop Control Model. Power Electron.*, Trondheim, Norway, 2016, pp. 1–9.
[34] Y. Jiang and A. Ekstrom, "General analysis of harmonic transfer through converters," *IEEE Trans. Power Electron.*, vol. 12, no. 2, pp. 287–293, Mar. 1997.
[35] K. Ilves, A. Antonopoulos, S. Norrga, and H.-P. Nee, "Steady-state analysis of interaction between harmonic components of arm and line quantities of modular multilevel converters," *IEEE Trans. Power Electron.*, vol. 27, no. 1, pp. 57–68, Jan. 2012.
[36] H. P. Mohammadi and M. T. Bina, "A transformerless medium-voltage STATCOM topology based on extended modular multilevel converters," *IEEE Trans. Power Electron.*, vol. 26, no. 5, pp. 1534–1545, May 2011.
[37] Q. Song, W. Liu, X. Li, H. Rao, S. Xu, and L. Li, "A steady-state analysis method for a modular multilevel converter," *IEEE Trans. Power Electron.*, vol. 28, no. 8, pp. 3702–3713, Aug. 2013.
[38] M. Beza, M. Bongiorno, and G. Stamatiou, "Analytical derivation of the AC-side input admittance of a modular multilevel converter with open- and closed-loop control strategies," *IEEE Trans. Power Del.*, vol. 33, no. 1, pp. 248–256, Feb. 2018.
[39] J. Lyu, Q. Chen, and X. Cai, "Impedance modeling of modular multilevel converter by harmonic linearization," in *Proc. IEEE 17th Workshop Control Model. Power Electron.*, Trondheim, Norway, 2016, pp. 1–6.
[40] J. R. C. Orillaza and A. R. Wood, "Harmonic state-space model of a controlled TCR," *IEEE Trans. Power Del.*, vol. 28, no. 1, pp. 197–205, Jan. 2013.
[41] J. Khazaei, M. Beza, and M. Bongiorno, "Impedance analysis of modular multi-level converters connected to weak AC grids," *IEEE Trans. Power Syst.*, vol. 33, no. 4, pp. 4015–4025, Jul. 2018.
[42] L. Jia, X. Ruan, W. Zhao, Z. Lin, and X. Wang, "An adaptive active damper for improving the stability of grid-connected inverters under weak grid," *IEEE Trans. Power Electron.*, vol. 33, no. 11, pp. 9561–9574, Nov. 2018.
[43] R. Mo, Q. Ye, and H. Li, "DC impedance modeling and stability analysis of modular multilevel converter for MVDC application," in *Proc. IEEE Energy Convers. Congr. Expo.*, Milwaukee, WI, USA, 2016, pp. 1–5.
[44] R. D. Middlebrook, "Input filter considerations in design and application switching regulators," in *Proc. IEEE Ind. Appl. Soc. Annu. Conf.*, 1976, pp. 366–382.
[45] J. Sun, "Impedance-based stability criterion for grid-connected inverters," *IEEE Trans. Power Electron.*, vol. 26, no. 11, pp. 3075–3078, Nov. 2011.
[46] F. Liu, J. Liu, H. Zhang, D. Xue, S. U. Hasan, and L. Zhou, "Stability issues of Z+Z or Y+Y type cascade system," in *Proc. IEEE Energy Convers. Congr. Expo.*, 2013, pp. 434–441.
[47] F. Liu, J. Liu, H. Zhang, and D. Xue, "Stability issues of Z + Z type cascade system in hybrid energy storage system (HESS)," *IEEE Trans. Power Electron.*, vol. 29, no. 11, pp. 5846–5859, Nov. 2014.
[48] B. Wen, D. Boroyevich, R. Burgos, P. Mattavelli, and Z. Shen, "Inverse Nyquist stability criterion for grid-tied inverters," *IEEE Trans. Power Electron.*, vol. 32, no. 2, pp. 1548–1556, Feb. 2017.
[49] Y. Liao and X. Wang, "Impedance-Based stability analysis for interconnected converter systems with open-loop RHP poles," *IEEE Trans. Power Electron.*, vol. 35, no. 4, pp. 4388–4397, Apr. 2020.
[50] K. Ji, G. Tang, J. Yang, Y. Li, and D. Liu, "Harmonic stability analysis of MMC-based DC system using DC impedance model," *IEEE J. Emerg. Sel. Topics Power Electron.*, to be published, doi: 10.1109/JESTPE.2019.2923272.

Zhenyu Li was born in Sichuan, China, in 1979. He received the Ph.D. degree in electrical engineering from Tsinghua University, Beijing, China, in 2007.

He is currently a Professor of engineering at State Grid Corporation of China, Beijing. His research interest includes high-voltage tech.

Zhang Wang was born in Zhejiang, China, in 1994. He received the B.S. degree from Beijing Jiaotong University, Beijing, China, in 2016, and the M.S. degree from Xi'an Jiaotong University, Xi'an, China, in 2019, both in electrical engineering.

His main research interests include modeling and control of multilevel converters and HVdc.

Yue Wang (Member, IEEE) was born in Liaoning, China, in 1972. He received the B.S. and Ph.D. degrees from Xi'an Jiaotong University, Xi'an, China, in 1994 and 2003, respectively, and the M.S. degree from Beijing Jiaotong University, Beijing, China, in 2000, all in electrical engineering.

He is currently a Full Professor with the School of Electrical Engineering, Xi'an Jiaotong University. His research interests include wireless power transfer, active power filters, multilevel converters, and HVdc.

Taiyuan Yin received the B.Eng. degree in electrical engineering from the Zhongyuan University of Technology, Zhengzhou, China. He is currently working toward the Ph.D. degree in electrical engineering from Xi'an Jiao Tong University, Xi'an, China.

His current interests include modeling and control of modular multilevel converter and stability analysis of modular multilevel converter-based high-voltage direct current systems.

Nian Mei was born in Hubei, China, in 1982. She received the Ph.D. degree in electrical engineering from the Huazhong University of Science and Technology, Wuhan, China, in 2009.

She is currently a Senior Engineer with State Grid Economic and Technological Research Institute CO. LTD. Her main research interests include voltage-source-converter-based high-voltage direct current, and line-commutated-converter based HVdc.

Bo Yue was born in Shaanxi, China, in 1976. He received the Ph.D. degree in electrical engineering from Xi'an Jiaotong University, Xi'an, China, in 2003.

He is currently a Senior Engineer with State Grid Economic and Technological Research Institute CO. LTD. His main research interests include high-voltage direct current, and high-voltage technology.

Wanjun Lei (Member, IEEE) received the B.S., M.S., and Ph.D. degrees in electrical engineering from Xi'an Jiaotong University, Xi'an, China, in 2000, 2004, and 2008, respectively.

He is currently an Assistant Professor with the School of Electrical Engineering, Xi'an Jiaotong University. His research interests include active power filters, power electronics inverters, reactive power compensation, and power quality control techniques.